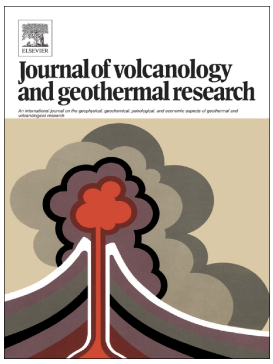

Magmatic evolution and textural development of the 1739 CE Pietre Cotte lava flow, Vulcano, Italy

Liam A. Bullock, Ralf Gertisser, Brian O'Driscoll, Sophie Harland

PII: S0377-0273(18)30295-6
DOI: https://doi.org/10.1016/j.jvolgeores.2019.01.017
Reference: VOLGEO 6536

To appear in: *Journal of Volcanology and Geothermal Research*

Received date: 16 July 2018
Revised date: 21 January 2019
Accepted date: 21 January 2019

Please cite this article as: L.A. Bullock, R. Gertisser, B. O'Driscoll, et al., Magmatic evolution and textural development of the 1739 CE Pietre Cotte lava flow, Vulcano, Italy, Journal of Volcanology and Geothermal Research, https://doi.org/10.1016/j.jvolgeores.2019.01.017

Magmatic evolution and textural development of the AD 1739 Pietre Cotte lava flow, Vulcano, Italy

Liam A. Bullock [a, b], *, Ralf Gertisser [a], Brian O'Driscoll [a, c], Sophie Harland [d]

[a] School of Geography, Geology and the Environment, Keele University, Keele, ST5 5BG, UK

[b] Ocean and Earth Science, National Oceanography Centre, University of Southampton, Southampton SO17 1BJ, UK

[c] School of Earth and Environmental Sciences, University of Manchester, Williamson Building, Oxford Road, Manchester, M13 9PL, UK

[d] School of Geosciences, Meston Building, University of Aberdeen, King's College, Aberdeen, AB24 3UE, UK

*Corresponding author: L.A.Bullock@soton.ac.uk

Abstract

Textural evidence from occurrences of mingled magmas in lava flows often yields insights into chemical and thermal disequilibrium between multiple magma batches at depth. An understanding of these interactions is key as they can occur on short timescales and may act as eruption triggers, particularly important in very active volcanic settings. This paper focuses on the Pietre Cotte lava flow (Vulcano, Aeolian Islands, Italy), a short (<1 km in length), texturally-heterogeneous rhyolitic extrusion on the northern slope of the active Fossa Cone. The occurrence of (i) multiple magma compositions, (ii) distinct magmatic cumulates (as glomerocrysts) and (iii) mineral resorption textures within glomerocrysts and isolated feldspar phenocrysts in the Pietre Cotte lava flow highlight a complex pre-eruptive magmatic history, including crystal mush remobilisation.

Petrographic observations and mineral, bulk rock and glass geochemistry suggest that multiple mingling events occurred during the evolution of the Pietre Cotte magmatic system, evidenced by the recognition of the following components: (1) a remobilised predominantly mafic crystal mush, evident as macrocrysts (crystals >500 μm), which form glomerocrysts within enclaves, (2) a microlitic (<100 μm) trachytic enclave groundmass with microcrysts (100-500 μm), and (3) a rhyolitic glass, which hosts both the enclaves and the glomerocrysts. The macrocrystic mafic assemblage includes clinopyroxene ($En_{38-47}Wo_{45-50}$; Mg# 0.72-0.89), olivine (Fo_{49-66}) and magnetite (Usp_{7-26}), with plagioclase ($An_{40-63}Ab_{5-50}$) and rare alkali feldspar (Or_{41-57}) also present. Enclaves are comprised of a groundmass of plagioclase (An_{43-47}) and alkali feldspar (Or_{33-57}) microlites, with clinopyroxene microcrysts ($En_{39-42}Wo_{47-51}$; Mg# 0.75-0.81) and trachyte groundmass glass. The rhyolitic host is characterised by glass, spherulites, microlites and enclave-derived macrocrysts.

Compositionally and texturally distinct magmas are attributed to storage and interactions of distinct magma batches and their cumulates at various temperatures and depths beneath the Fossa Cone. Compositions vary from basaltic-shoshonitic, through latitic-trachytic and rhyolitic magmas. The macrocrystic glomerocryst assemblage shows resorbed, chemically-zoned and cumulate textures; the glomerocrysts are attributed to a shoshonitic parent and remobilisation from a crystal mush. Macrocrysts formed at a pressure of 825 ±80 MPa and temperatures of 789-1117°C at around the Moho (~23-28 km). Pressure and temperature calculations of the shoshonitic mineral assemblage give average crystallisation conditions of 710 ±80 MPa (above the Moho) and 1128 ±25°C, respectively. The trachytic magma crystallised at ~640 ±75 MPa and 1000-1130°C. The average liquidus of the rhyolitic magma has been calculated at 970 ±7°C, at depths of <5 km (<60 MPa). New textural observations and intensive variable calculations permit the development of a new pressure and temperature-constrained model of the magmatic evolution of the Pietre Cotte system prior to eruption, with useful insights into the interactions of different magmatic components prior to and during the rapid onset of eruptions linked to magma mingling/mixing.

Keywords: Pietre Cotte, Vulcano, rhyolite, trachyte, magma mingling, magmatic cumulates

1. Introduction

Magma mingling processes can play an important role in the textural evolution of a magmatic system, resulting in chemical and thermal disequilibrium between juxtaposed components (Anderson, 1976; Morgavi et al., 2016). The injection of a more mafic magma into a felsic magma can also act as a trigger for highly explosive volcanic eruptions (Sparks et al., 1977; Murphy et al., 1998; Leonard et al., 2002; Perugini and Poli, 2012; Morgavi et al., 2016). The study of mixed and/or mingled magmatic systems is important for monitoring activities and hazard assessment in active volcanic regions; as such mingling-to-eruption events may occur on a timescale ranging from years to minutes (Ruprecht and Plank, 2013; Perugini et al., 2015; Petrelli et al., 2018). The Pietre Cotte rhyolite lava flow (AD 1739) on the northern slope of the active Fossa Cone (Vulcano, Aeolian Islands, Italy; Fig. 1) preserves textural evidence for several stages of pre-eruptive processes, including magma mingling, providing an ideal system to investigate magma plumbing system dynamics. Mingling of evolved magma compositions has been identified in the Rocche Rosse rhyolitic lava flow on the neighbouring island of Lipari, Aeolian Islands (Davì, 2007; Davì et al., 2009, 2010; Forni et al., 2015). The Rocche Rosse flow contains latitic-to-trachytic enclaves, originating from a deeper basaltic-shoshonitic chamber. The interaction of the shoshonitic magma with trachytic and rhyolitic magmas residing in the crust may have triggered the Rocche Rosse eruption of

1230 ±40 AD (Davì, 2007; Davì et al., 2009, 2010; date determined by archaeomagnetic dating of Arrighi et al. 2006). Similar compositions and mingling textures have been identified in young rhyolitic lava flows on Vulcano, including the AD 1739 Pietre Cotte lava flow (Frazzetta et al., 1984; De Astis et al., 1997, 2013; Piochi et al., 2009; Forni et al., 2015; Vetere et al., 2015; Nicotra et al., 2018).

Although extensive work has been undertaken on the Pietre Cotte magmatic system (Perugini et al., 2007; Piochi et al., 2009; Forni et al., 2015; Vetere et al., 2015; Nicotra et al., 2018), contrasting models exist on the conditions and textural evolution of enclaves within the rhyolitic host. It is not yet clear how the primary magma differentiated, how glomerocrysts are were entrained into the enclave magma, how many magmas interacted and at what depths in the pre-eruptive magma plumbing system these interactions occurred. Previous studies have addressed the magma chamber dynamics associated with the later stages of evolution of the Pietre Cotte lava flow (Perugini et al., 2007; Piochi et al., 2009; Forni et al., 2015; Vetere et al., 2015). Piochi et al. (2009) modelled the processes of magma evolution based on field, textural and fractal data, major, trace and volatile element analyses, and incorporated petrological and fluid inclusion data from De Astis et al. (1997), Gioncada et al. (1998) and Frezzotti et al. (2004). Piochi et al. (2009) suggested a genetic relationship between the two magmas involved through assimilation and fractional crystallisation (AFC), with mingling of an uprising rhyolitic magma and a shallower latitic-trachytic plug, followed by separation of latitic-to-trachyte enclaves (SiO_2 = 57–63 wt.%) within the rhyolite. A juvenile origin for the enclaves was proposed based on their dominantly subcircular shape, the occurrence of enclave-type veins in the rhyolite and vesicularity within the enclaves. The sharp contact between the rhyolitic host and enclaves was suggested to imply the absence of significant elemental diffusion, with physical mingling, rather than mixing, the dominant process between the two magmas. Piochi et al. (2009) calculated the depth of formation of Si-rich melts (formed in association with a shoshonitic melt) at >2200 bar, with a lati-trachyte formed at lower pressure of ~300 bars and temperatures of 1050–1080°C. Magma mingling occurred at shallower depths with a pressure range of 600–300 bars (Piochi et al., 2009). A lati-trachytic plug was envisaged by the latter authors, with contemporaneous eruption of the lati-trachytic and rhyolitic magmas caused by the rise of the rhyolitic magma. Desegregation of the partially solidified plug accounts for mingling at variable scales and the fragmented nature of the enclaves (Piochi et al., 2009).

Perugini et al. (2007) and Vetere et al. (2015) proposed that enclaves formed within the rhyolitic host by injection of the latitic-to-trachytic enclave magma into the rhyolitic magma. This is based on enclave morphology and size distribution analysis; fragmentation processes ensued in response to disruption of viscous fingering morphologies, caused by rheological contrasts between

the enclave magma and the rhyolitic magma. Vetere et al. (2015) used thermodynamic and rheological modelling to explain the variability of observed viscosity ratios, a product of a large volume of enclave magma intruding a smaller volume of rhyolitic magma, resulting in viscous fingers of enclave magma in the rhyolitic host. The compositionally similar 1888-1890 Vulcano eruption products were interpreted as the reactivation of a latitic magma, possibly evolving to produce trachytic-to-rhyolitic compositions. Vetere et al. (2015) also observed variable enclave shapes, from highly-convoluted to near-rounded. Forni et al. (2015) examined the composition and magmatic history of erupted cumulate fragments in the rhyolites on Lipari and Vulcano. The authors noted that, while the Pietre Cotte lava flow is considered to be representative of a latitic-to-trachytic magma interacting with a rhyolite, the crystallisation of Sr-rich plagioclase from latitic-to-trachytic magma would require extremely high plagioclase/melt partition coefficients for Sr, or extremely high Sr contents in the melt. A remobilised cumulate was suggested as sourcing the crystal-rich enclaves within Lipari rhyolitic products but this has thus far only been speculated to be the case for the Vulcano rhyolites (Forni et al., 2015).

Remobilised cumulates are being increasingly recognised in large crystal-poor rhyolite systems worldwide (typically 5 km^3 to >5000 km^3, e.g. Bachmann and Bergantz, 2003, 2004; Shane et al. 2005; Wolff et al., 2015), and have also been identified in small volume systems (typically <5 km^3, e.g. Wörner and Schmincke, 1984; Spell et al., 1993; Geist et al., 1995; Bacon et al., 2007; Shane et al., 2008). Macrocrystic (used here refer to crystals >500 μm in size) mafic minerals which often make-up glomerocrysts in the Pietre Cotte enclaves and the rhyolitic host have been previously identified as phenocrysts, crystallised from a magma with an intermediate composition to form the enclaves (Vetere et al., 2015). However, if these glomerocrysts in fact represent a remobilised crystal mush, this may offer new insights into the early stages of magmatism prior to eruption of the Pietre Cotte lava flow. In systems of interacting cumulates and magmas, bulk rock geochemistry reflects an average composition of multiple magmas that may mask complex interaction histories (Leeman and Hawkesworth, 1986; Waight et al., 2000). Therefore, the textural relationships are important for unravelling the story of complex magma interactions.

The aim of this paper is to further constrain the processes of textural evolution and shoshonite, trachyte and rhyolite magma genesis in the Pietre Cotte system. We present new textural and geochemical data to model the evolution of the system, from the initial stages of crystallisation and mineral/melt phase interactions at different depths below the Fossa Cone, up to the eventual eruption level. Cumulates, enclave groundmass and the rhyolitic host record different evolutionary stages that led to the texturally heterogeneous Pietre Cotte lava flow. This contribution offers a new model for the evolution of the Pietre Cotte system, including observations of the early

stages of crystal mush-enclave magma interaction at depths reaching the Moho (~21-25 km, Falsaperla et al., 1985; ~18-20 km, De Astis et al., 2013), a discussion of the interaction between the enclave-forming magma with the rhyolitic host at shallower crustal depths, and thermobarometric constraints on the stages of textural evolution. The new model presented here proposes that a shoshonitic to latitic-trachytic magma mingled with a crystal mush, itself remobilised by a mafic input, at depths close to the Moho, before rising and mingling with a shallower rhyolitic magma. Deeper, lower crustal magma evolution, and interactions during migration with shallower crustal batches, may lead to rapid onset eruptions in active areas such as the Lipari-Vulcano volcanic system. This is highly important for hazard assessment.

2. Regional geological setting and eruption history of the Fossa Cone

The Aeolian volcanic arc forms a ring-shaped chain of volcanic islands and seamounts above the south Tyrrhenian subduction zone (Tyrrhenian Sea, southern Italy; Fig. 1a). Vulcano sits on top of ~20 km crust, consisting of the metapelitic Calabrian arc, a felsic granulitic upper crust and mafic granulitic lower crust (Milano et al., 1989; Wang et al., 1989; Ventura et al., 1999; Peccerillo et al., 2006; De Astis et al., 2013). Vulcano is a relatively young island (~127 ka; Keller, 1980; De Astis et al., 2013), constructed through time by the lavas and pyroclastic products of four volcanic centres – Primordial Vulcano (high-K calc-alkaline basaltic andesite to andesite), the Lentia Complex (latite to rhyolite), the Fossa Cone (latitic to rhyolite) and Vulcanello (potassic alkaline shoshonite-latite-trachyte) (Keller, 1980; De Astis et al., 1997; 2006; 2013; Del Moro et al., 1998). The most recent eruptive epoch is defined by the continual development of the Gran Cratere di La Fossa (latitic, trachytic and rhyolitic in composition) and Vulcanello. The active Fossa Cone is located within the Fossa Caldera (Northern Vulcano; Fig. 1b-d). The composite Fossa Cone has been active since ~5.5 ka (Frazzetta et al., 1984), made up of pyroclastic sequences and lava flows during successive eruptive phases (Arrighi et al., 2006; Di Traglia, 2011; De Astis et al., 2013). The Pietre Cotte lava flow is dated at 1739 AD by historical records (De Fiore, 1922; Keller, 1970; Frazzetta et al., 1984; De Astis et al., 2013), in agreement with an age of 1720 ±30 AD by archaeomagnetic dating (Arrighi et al., 2006). The last eruption at the Fossa Cone occurred at 1888-1890, with the emission of pyroclastic material, giving rise to the typical "Vulcanian" eruptive style first described at this location (Mercalli and Silvestri, 1891; Keller, 1980; Dellino and La Volpe, 1997; Peccerillo et al., 2006; De Astis et al., 2013).

Eruptions at the Fossa Cone are fed by dyke-like caldera pathway structures, allowing for magma ascent independent of the regional stress field (Ruch et al., 2016). A well-structured shallow (close-conduit) feeder system of small batches of latitic magmas (fed by a deeper, basaltic-

shoshonitic magma) is suggested for beneath the Fossa Cone (Paonita et al., 2013; Mandarano et al., 2016), hypothesised to feed fumarolic emissions at the crater (Paonita et al., 2013). A magma of latitic-to-trachytic composition has been commonly suggested as the origin for the Pietre Cotte enclaves (Keller, 1980; Piochi et al., 2009; Vetere et al., 2015; Nicotra et al., 2018). Abundant enclaves within the Pietre Cotte lava flow contain a macrocryst assemblage comprising plagioclase, clinopyroxene, olivine and magnetite, with a plagioclase and alkali feldspar microlitic (<100 μm) groundmass, and clinopyroxene microcrysts (100-500 μm) within the groundmass. Previous models proposed for the evolution of the Pietre Cotte magmatic system constrain the conditions of the interaction between the enclave magma and the rhyolitic host, leading to the eventual effusive eruption.

3. Methods

3.1. Enclave morphology

Enclaves were identified and morphologically analysed from outcrop examples (Table 1, Fig. 6 and Supplementary Material 1). In total, 968 enclaves were analysed for shape, size and area based on field observations and photographs (see Supplementary Material 1). Enclave shape analysis was based on detailed, close-up photos of 228 enclaves (examples shown in Fig. 2, see also Table 1 and Supplementary Material 1) and eight outcrop overview photographs of 740 enclaves. Size and area statistics were based on the outcrop overview photographs only.

The analysis of fabric anisotropy was applied to two dimensional images of enclaves in order to determine preferential shape orientation of different enclave types. The method is based on the counting of a number of intercepted segments of a set of objects on the image by a set of parallel scan lines along a number of orientations (Launeau et al., 1990; Launeau and Robin, 1996). Rose diagrams and best fit ellipsoids (characteristic shape profile) serve to quantify the fabric, its symmetry and number of intercepts in each direction. A linear filter minimises the effects of grid anisotropy on the counting of intercepts. Rose diagrams were created using ImageJ (Ferreira and Rasband, 2012; Schneider et al., 2012) and CSDCorrections 1.37 (Higgins, 2000; 2002; 2006), and preferred orientation (best fit ellipsoid) profiles were created using Intercepts 2003 software (Launeau and Robin, 1996). The intercept counting method was applied to scaled and orientated field images of enclaves to highlight any preferential axes orientation. This method permits interpretations to be made of the rheology of interacting phases, and the possible effects of magma ascent and flow emplacement. A comprehensive and critical review of the method of Intercepts is

provided by Launeau and Robin (1996). CSDSlice (Morgan and Jerram, 2006) and MATLAB® 6.1 commercial software were also used to create a best fit for the aspect ratios, giving X, Y and Z values (defining the plane in a 3D space) and 3D visual representations of enclave shape.

3.2. Scanning Electron Microscopy

Rhyolite host and enclave samples (typically <20 cm in diameter) were collected in-situ at sites across the Pietre Cotte lava flow. Rhyolitic host lava, magmatic enclaves and glomerocrysts were examined using an ISI ABT-55 scanning electron microscope (SEM) (Kevex, Thermo Fisher Scientific) with Link Analytical 10/55S EDAX (EDS) facility for mineralogical determination. Backscatter electron (BSE) imaging and EDS analyses were performed on polished thin sections at 15 kV using a 60 µm aperture and beam (probe) current of 1.80 nA.

3.3. Glass, whole rock and mineral chemistry

Glass and mineral major element analysis was undertaken on polished thin sections of enclaves and host lava at The Open University (UK) using a CAMECA SX 100 electron microprobe (EMP). For EMP analysis (EMPA), the peak count per element for analyses was 15 s (background) to 30 s (peak) using a 10-20 µm defocused beam diameter for glass, with an acceleration voltage of 15 kV and a beam current of 20 nA. A 1 µm wide beam was used for minerals at a count time of 30 s per element. Certified volcanic glass (VG-568 and KN-18) and appropriate mineral standards were systematically analysed as secondary standards. A subset of twenty-two whole-rock samples (fourteen enclave material, eight rhyolitic host lava) was selected for major element analysis by inductively coupled plasma atomic emission spectrometry (ICP-AES), and for trace element analysis by inductively coupled plasma mass spectroscopy (ICP-MS), using Agilent instruments at OMAC Laboratories, Loughrea, Ireland (Agilent 5100 Series ICP-AES and Agilent 7700 Series ICP-MS). Each sample was milled and homogenised, with 0.25 g digested with aqua regia in a graphite heating block. The residue was diluted with deionised water, mixed and analysed. Results were corrected for spectral inter-element interferences. Calibration was based on two reference materials (OREAS-121 uranium ore certified reference material (CRM) and AMIS0304 carbonatite CRM), using recommended element concentrations. Duplicate analyses of two CRMs and two randomly selected samples produced reported values within the acceptable range for laboratory replicates, with a mean relative difference of 4%. Duplicate analyses included samples processed through the entire analytical procedure.

3.4. Thermobarometry and geochemical modelling

Several studies have identified multiple connected magma reservoirs beneath the Fossa Cone down to the crust-mantle boundary, hosting magmas ranging in composition from basalts to rhyolites (Clocchiatti et al., 1994; Paonita et al., 2002; 2013; Zanon et al., 2003; Peccerillo et al., 2006; Piochi et al., 2009; De Astis et al., 2013; Mandarano et al., 2016; Nicotra et al., 2018). Therefore, several thermobarometric models have been applied in this study to calculate magmatic crystallisation conditions for different reservoir depths. This includes calculations of: (1) the potentially deepest conditions, represented by predominantly mafic (with plagioclase and minor alkali feldspar) macrocryst assemblages (manifested as glomerocrysts), (2) lower crustal conditions, where shoshonitic, latitic and trachytic magmas may reside and crystallise, (3) mid- to upper crustal conditions, where latitic to trachytic magmas reside, and (4) shallow crustal conditions, where the rhyolitic host magma formed.

Deep storage intensive variables corresponding to olivine, clinopyroxene and magnetite glomerocryst formation were calculated by QUILF thermometry, performed using the QUILF95 software (Andersen et al., 1993). The program was used for temperature determinations based on Fe-Mg-Ca exchange between clinopyroxene, olivine and magnetite in equilibrium (Frost et al., 1988; Lindsley and Frost, 1992; Frost and Lindsley, 1992; Andersen et al., 1993). Unaltered (non-exsolved) crystal cores from touching glomerocryst-hosted crystals (assumption that neighbouring crystals are in equilibrium) were selected for analysis for equilibrium assemblages, using an average mineral composition from analysed olivine (n=33), clinopyroxene (n=47) and magnetite (n=61) crystals considered to be in equilibrium. A pressure input was calculated using the clinopyroxene-composition barometer of Putirka (2008) (see below) for glomerocryst-hosted clinopyroxene crystal compositions.

Lower crustal conditions for potential shoshonitic to trachytic magmas were calculated by clinopyroxene-composition and clinopyroxene liquid modelling (Putirka, 2008). These models are considered to be among the most versatile available, used in numerous magma plumbing system studies (e.g. Schwarz et al., 2004; Stroncik et al., 2009; Hildner et al., 2011; Dahren et al., 2012; Jeffery et al., 2013; Barker et al., 2015). Clinopyroxene-composition models were used to calculate and constrain pressure in hydrous melts, using jadeite-diopside/hedenbergite exchange equilibria, using modelling techniques recalibrated by Putirka (2008) from barometry developed by Nimis (1995) and Nimis and Taylor (2000). Clinopyroxene composition thermobarometry can be applied independently of a co-existing melt for calculations, which is beneficial in complex systems like

Pietre Cotte where disequilibrium textures and multiple magma batches are evident. A broad temperature range of 800-1200°C was input, with a minimum H_2O content of 0.45% water used, consistent with a mean shoshonitic water content calculated from the values of Gioncada et al. (1998), later also used by Nicotra et al. (2018). FTIR basaltic (La Sommata) melt inclusion data from Clocchiatti et al. (1994) show H_2O contents of up to 3.8%, with calculated values of 0.3-0.6% for shoshonitic compositions and between 0.8 and 1.9% for latitic compositions. A maximum parental magma H_2O content of 3.8% has therefore also been used for the calculations. Liquid compositions utilised for temperature estimates include shoshonitic-to-latitic compositions from previous studies (De Astis et al., 1997; 2013; Del Moro et al., 1998; Gioncada et al., 1998) and trachytic compositions from this study. A crystallisation pressure range of 110 to 850 MPa was used for calculations in order to cover a depth from the deepest inferred rhyolitic magmas to the deepest mafic magmas in the lower crust. Microcrysts of clinopyroxene were selected for thermobarometric modelling, with crystal cores used to constrain mafic compositions (representative of a shoshonitic magma), and rims for latitic to trachytic compositions.

Mid- to upper crustal conditions of an equilibrated plagioclase-alkali feldspar groundmass in a trachytic magma were calculated by SOLVCALC (Wen and Nekvasil, 1994). This method was used to constrain equilibrium and temperature conditions for coexisting alkali feldspar and plagioclase in the trachytic enclave groundmass, with estimates of stepped pressure (400-800 MPa) and temperature (800-1200°C) intervals applied (Nekvasil and Burnham, 1987). Equilibrium of plagioclase and clinopyroxene crystals with a shoshonitic, latitic and trachytic magma was further substantiated by using the equilibrium tests of Putirka (2008), using the same pressure and temperature parameters. This method works by comparing a co-existing melt using An-Ab exchange (for plagioclase) and Fe-Mg exchange coefficient (for clinopyroxene) with constant values (Putirka et al., 1996; Putirka, 1999; Putirka, 2008). The equilibrium constant is sensitive to temperatures at T<1,050°C (the output value should be ~0.1 ±0.11 for temperature systems above 1,050°C, or equal ~0.25 ±0.05 for temperature systems below 1,050°C). These tests have been applied for clinopyroxene with co-existing shoshonitic, latitic and trachytic magma compositions (De Astis et al., 1997; 2013; Del Moro et al., 1998; Gioncada et al., 1998), as well as trachytic and rhyolitic (the latter for plagioclase only) glass compositions from this study.

Shallow upper crustal rhyolitic conditions were calculated by Rhyolite-MELTS thermometry (Gualda et al., 2012). Rhyolite-MELTS was used for the storage conditions of the rhyolitic host as the method permits more accurate modelling of rhyolitic chemical systems compared to Pele 8.00 and MELTS (Ghiorso and Sack, 1995; Boudreau, 1999; Gualda et al., 2012). Rhyolite-MELTS facilitates thermodynamic modelling of phase equilibria in hydrous silicic systems over a range of temperatures

500-2000°C and pressures 0-2 GPa. Rhyolite-MELTS differs from the MELTS calibration (Ghiorso and Sack, 1995; Asimow and Ghiorso, 1998) as the enthalpies of formation of quartz and end member $KAlSi_3O_8$ in feldspar solid solution have been adjusted.

Projected fractional crystallisation (FC) and assimilation and fractional crystallisation (AFC) curves were calculated using the FC–AFC–FCA (decoupled FC-AFC) and mixing modeller Microsoft® Excel© spreadsheet program of Ersoy and Helvaci (2010). This was undertaken in order to model the evolutionary processes of rhyolitic host composition development using whole rock shoshonitic and rhyolitic trace element compositions, and a Calabro-Peloritano basement assimilant (Frezzotti et al., 2004). Input parameters used in FC-AFC modelling are available in Supplementary Material 2.

4. Results

4.1. Field observations and enclave morphology

The base of the Pietre Cotte cyclic unit consists of ash and pumice layers (up to 3 m thick; De Astis et al., 2013), followed by the Pietre Cotte lava flow, covered sporadically by finely laminated and lenticular massive ash layers (Gran Cratere Formation, 2-4 m thick trachy-rhyolites; De Astis et al., 2013). The tongue-shaped flow is up to 20 m thick at the flow front, and is characterised by spherulites, flow foliations, folding, a blocky surface and enclaves (also described by Piochi et al., 2009; De Astis et al., 2013; Bullock et al., 2017). Enclaves are dark-red to purple in colour, and are typically ellipsoidal, though some show more angular morphologies (Perugini et al., 2007; Piochi et al., 2009; Vetere et al., 2015). The total volume of the Pietre Cotte lava flow has been previously estimated to be 2.4×10^6 m^3 (Frazzetta and La Volpe, 1991), with enclaves representing 5-6% of the total volume of the flow (Vetere et al., 2015). Enclaves are widespread across flow extent and vary in size from a few mm up to 30 cm in diameter. Two enclave types are distinguished based on their typical shapes: rounded enclaves and angular enclaves. The majority of enclaves (79%) are rounded, with cuspate, crenulated and lobate contacts against the rhyolitic host (Fig. 2). The remaining 21% of analysed enclaves show more angularity, i.e. straight boundaries and sharp corners (Fig. 2). Based on field observations and microscopic imagery, three textural distinctions have been recognised in the Pietre Cotte lava flow: (1) Rhyolitic obsidian glass (rhyolitic host; Fig. 3a), (2) Microlitic groundmass (<100 µm) to microcrystic (100-500 µm, typically up to 200 µm) enclave material (Fig. 3b), and (3) macrocrysts and glomerocrysts, present in enclaves and also separated out into the rhyolite host (Fig. 3c). There are a number of notable textural features at the contacts between the enclaves and the rhyolite host (Fig. 4b). There is some evidence of chilled margins and finer-grained enclave

groundmass at enclave edges compared to their centres (Fig. 4). The edges of enclaves show crenulated, cuspate boundaries, with a higher abundance of vesicles also apparent at the enclave-host interface (Fig. 4c-f).

Overall, measured enclaves occupy ~4.4% by volume of the total rhyolitic host lava area investigated here (Table 1). The average diameter of analysed enclaves is 33.5 mm, with an average perimeter of 87 mm, though there are numerous examples of larger enclaves across the flow based on field observations. Enclaves are typically sub-spherical, with an average overall circularity index of 0.89 (an index value of 1 represents a perfect spheroid; Table 1). As anticipated, more rounded enclaves have a higher circularity index value (0.92 compared to 0.82 for more angular enclaves), while angular enclaves have a larger diameter (averaging 41 mm compared to 33 mm for rounded enclaves) and perimeter (107.5 mm compared to 86 mm). Rounded enclaves comprise a higher proportion of the rhyolitic host compared to more angular enclaves (6.3% compared to 1.1%; Table 1). Morphological calculations (Fig. 6a) indicate there is not a significant quantifiable shape variation in the more spherical and more angular enclaves observed in the field. Based on representative short, intermediate and long axes ellipsoid calculations, both angular and rounded enclaves show overall roughly sub-spherical (equant) shapes (Fig. 6b), with some deviation in the length to width aspect ratio with increasing enclave size (Fig. 6a). The slight differences in solidity and circularity values (departure from an ideal model sphere value of 1; Table 1), and the representative rose diagrams and best fit ellipsoids (Figs. 6c-d), suggest that more rounded enclaves have a higher degree of concavity and more boundary irregularities than more angular enclaves. Both angular and rounded enclaves show a preference for a slight flat long axis preferred orientation (parallel to base of flow in outcrop), as evident by the rose diagrams (Fig. 6c) and best fit ellipsoids (Figs. 6d-e).

4.2. Petrography and geochemistry

Glass, whole rock and mineral chemical data are available in Tables 2-6. All mineral compositions are available in Supplementary Material 2. Fig. 7 shows the range of Pietre Cotte, Fossa Cone and other Vulcano suite compositions (Caruggi Fm (Commenda), Grotta dei Palizzi Fm, Punte Nere Fm, Monte Saraceno Fm, Piano Grotte dei Rossi Fm, Gran Cretere Fm, Vulcanello Fm, La Sommata Fm, Monte Rosso Fm, Punta di Mastro Minico Fm and Monte Lentia Fm) from this and previous studies, spanning basalt to rhyolite (De Astis et al., 1997; 2013, Del Moro et al., 1998, Gioncada et al., 1998; Piochi et al., 2009; Nicotra et al., 2018). Enclaves and the rhyolitic host exhibit negative Nb-Ta-P-Ti anomalies (Fig. 8), typical of subduction-related magmas (Pearce, 1982; Baier et al., 2008). The rhyolitic host shows negative anomalies of Ba, Nb, Sr and Zr, and positive anomalies of Th and U. The

rhyolitic host also shows a pronounced negative Eu anomaly in the rhyolitic host REE plot (Eu/Eu* ~0.10 based on $Eu_N/(S_N*GdC_N)^{0.5}$), calculated according to the equation of McLennan (1989). Major element Harker diagrams of TiO_2, Fe_2O_3, MgO and CaO abundances show an overall and continuous decrease with increasing SiO_2 (Fig. 9). Major element oxides Al_2O_3, Na_2O, K_2O and P_2O_5 show a peaked trend, increasing up to trachytic compositions, and decreasing to rhyolitic compositions. Rubidium continuously increases with increasing SiO_2, and, Zr and Nb tend to increase with increasing SiO_2 content, followed by a decrease at rhyolitic compositions (Fig. 10). Vanadium is inversely correlated with SiO_2, while Ba and Sr show peaked trends, increasing to trachytic compositions before decreasing to rhyolitic compositions.

4.2.1. Rhyolitic host lava

The rhyolitic host lava (excluding enclaves) is variably glassy (~70%), devitrified (~25%) and microcrystalline (~5%), predominantly displaying a dull black lustre to a light grey colour (Fig. 2). Glass compositions from the Pietre Cotte lava host are rhyolitic, exhibiting a SiO_2 range of 73.2-77.5 wt% and total alkali contents of 6.6-9.3 wt% (n=24; Figs. 7a-b). The rhyolitic host shows REE compositions similar to other Fossa Cone products (De Astis et al., 1997, 2013; Gioncada et al., 1998; Del Moro et al., 1998; Piochi et al., 2009; Nicotra et al., 2018). Rhyolitic obsidian glass contains macrocrystic (typically 500 μm), predominantly mafic crystals (clinopyroxene, olivine, magnetite), plagioclase and rare alkali feldspar, often surrounded by a thin layer of groundmass material similar to enclaves (Fig. 3b). The rhyolitic host is predominantly crystal-poor, containing a minor antecrystic macrocryst assemblage of plagioclase, clinopyroxene, alkali feldspar, olivine and magnetite. The antecrysts occur individually or as glomerocrysts (Fig. 3c). No phenocrysts (free of any enclave-derived surrounding groundmass) were identified in the rhyolitic host. Spherulites are widespread in the obsidian glass, occurring individually, in clusters and concentrated in bands (Bullock et al., 2017). Spherulites also nucleate at the edges of enclaves, touching and wrapping enclave borders, and vesicles also surround enclaves (Vetere et al., 2015). Microlites (plagioclase, alkali feldspar and clinopyroxene) are also widespread, often showing a parallel alignment, defining the primary flow foliation. The microlite foliation may be deflected around, or remain unchanged, close to spherulites (Bullock et al., 2017). Plagioclase microlites within the rhyolitic host exhibit a broad compositional range of An_{5-46}, while alkali feldspar microlites show a range in composition of Or_{9-57}.

4.2.2. Enclave groundmass

The groundmass of the enclaves is predominantly fine-grained microlitic and isotropic (Fig. 3b). Individual laths are typically 30-40 µm in length (Fig. 3d), though there are patches of coarser-grained groundmass material within enclaves, with individual crystals of 80-100 µm in length (Fig. 4). The enclave groundmass is formed of alkali feldspar and plagioclase, with abundant antecrystic macrocrysts and glomerocrysts. Interstitial brown glass (typically <10% of the enclave volume) is evident within the enclave groundmass, also identified by Piochi et al. (2009). Glass is spatially associated with vesicular areas at the edges of enclaves (Fig. 4c, 5c, 5e) and in rims around macrocrysts (Fig. 5c). Microcrysts (typically up to 200 µm in diameter) of subhedral clinopyroxene are evident within the groundmass. Whole rock enclave compositions (together with glomerocryst material) plot on the boundary between basaltic andesite and basaltic trachyandesite (TAS diagram, composition (SiO_2 content = 51.9-53.3 wt%, total alkali content = 4.2-4.5%; n=14; Fig. 7a), and mostly plot as shoshonites related to the shoshonite series (K_2O vs. SiO_2 classification diagram of Peccerillo and Taylor, 1976; Fig. 7b). These whole rock enclave compositions are herein referred to as shoshonites. Enclave groundmass glass (EMPA) compositions plot as trachytes in the TAS diagram (SiO_2 content = 60.7-63.5 wt%, total alkali content = 8.2-10.9 wt%, n=12; Fig. 7a), and show predominantly latite to trachyte (and rare andesite-dacite high-K calc-alkaline) compositions of the shoshonite series (Fig. 7b). Enclave groundmass glass compositions are herein referred to as trachytes (consistent with their classification on Fig. 7a and maximum achieved classification on 7b).

4.2.3. Macrocryst assemblage and glomerocrysts

The rhyolite host lava and enclaves both contain macrocrystic plagioclase (~50% of observed minerals), clinopyroxene (~20%), alkali feldspar (~15%), magnetite (~10%) and olivine (~5%). This mineral assemblage, more mafic than the lava host, often manifests as interlocking crystals forming glomerocrysts (Fig. 3c). Biotite has also been previously identified in association with macrocrysts in the Pietre Cotte enclaves (Perugini et al., 2007; De Astis et al., 2013). Rare apatite was identified and has been previously noted as an accessory phase (<0.1 vol.%) in Pietre Cotte rhyolite and enclaves (Piochi et al., 2009), as well as in older shoshonites, trachytes and other mafic-intermediate rocks from the Vulcano suite (Del Moro et al., 1998; Frezzotti et al., 2004; De Astis et al., 2013). This mineral assemblage occurs more frequently within enclaves than within the rhyolitic host.

The mineral assemblage is comparable to that found in deposits of shoshonitic and latitic compositions on Vulcano (De Astis et al., 2013). Resorption and zonation is evident in plagioclase (Fig. 5a-f) and clinopyroxene (Fig. 5g-h) macrocrysts, with typically coarser-grained groundmass surrounding the macrocrysts (Fig. 5b). Rare prismatic, unzoned plagioclase (~1-2 mm) occurs within

finer-grained enclave groundmass (Fig. 5c), while in coarser-grained patches of groundmass, some plagioclase crystals show internal resorption and others show normal zonation (Figs. 5a-b, d, f). Many prismatic plagioclase crystals show higher Ab content in their rims compared to their cores (identified by EDS; Fig. 5a), or show alkali feldspar overgrowths (Fig. 5d-e). Macrocrystic feldspars within enclaves are predominantly plagioclase, but the groundmass is mostly made up of alkali feldspar (Fig. 12a), with some larger pristine alkali feldspar crystals also evident. Both resorbed (typically 5 to 15 mm) and euhedral (typically up to 5 mm) plagioclase crystals are identified in enclaves. Rare xenocrysts of plagioclase up to 15 mm in size have also been previously noted in the Pietre Cotte enclaves by Mandarano et al. (2016) and Nicotra et al. (2018), with the latter describing their occurrence in detail, showing plagioclase crystals exhibiting resorbed cores and dissolution textures. All plagioclase crystals are labradorite and andesine ($An_{40-63}Ab_{5-50}$; Fig. 11a) in composition, with occasional sanidine (Or_{41-58}) too (Figs. 5a-e). The composition of resorbed plagioclase differs slightly from that of euhedral crystals, with resorbed plagioclase showing a compositional range of An_{48-64} (average content of An_{53}), compared to An_{5-50} (average An_{42}) for euhedral crystals. Plagioclases with low An compositions have been previously identified in older Fossa products (Punte Nere Formation pyroclastic products with An_{19}; De Astis et al., 2013).

Clinopyroxene (~500 µm to 1 mm in length) exhibits zonation and resorption, with magnetite inclusions at the crystal edge, particularly in the coarser enclave groundmass (Fig. 5f). Clinopyroxene often occurs as inclusions in plagioclase. Macrocrystic clinopyroxenes are diopsidic in composition ($En_{38-47}Wo_{45-50}$; Mg# = 0.72-0.89; n=47; Fig. 11b). Zoned clinopyroxenes have been identified, with rims showing a slightly elevated Mg# (0.77 to 0.89, average Mg# 0.81) compared to cores (0.72-0.8, average Mg# 0.77). Clinopyroxene En and Wo compositions show some overlap with previously measured older (Epochs 1-6) shoshonitic compositions (De Astis et al., 2013). Magnetite and olivine (~500 µm) occur in glomerocrysts with clinopyroxene, as well as individually, in clusters or as inclusions. Magnetite crystals are titaniferous in composition (Usp_{7-26}; n=61; Fig. 12c) and olivine phenocrysts contain a forsterite range of Fo_{49-66} (n=33; Fig. 12b). Forsterite contents of latite-derived olivine crystals have been previously reported as Fo_{55-72}, while shoshonite-derived olivine crystals are Fo_{60-78} (Gioncada et al., 1998). Samples of the Passo del Piano Fm mafic lava and the Carrugi Fm (Palizzi-Commenda eruptive cycle) porphyritic latitic lava contain olivine crystals which show a forsterite content range of Fo_{57-81} (Mandarano et al., 2016). Other previously measured olivines (in Epoch 6-8 latites, including examples which are noted to exhibit disequilibrium textures) have low forsterite contents (Fo_{44}) (Punta del Roveto lava flow (Vulcanello) groundmass olivine; De Astis et al., 2013).

5. Discussion

Given the wide range in enclave compositions and texturally distinct and variably disequilibrated crystals, it is clear that the Pietre Cotte magma underwent a complex and stepped magmatic evolution before eventual lava flow extrusion. Different magma storage conditions and interactions are discussed below.

5.1. Intensive variables

Calculated intensive variables are shown in Table 7 (see also Supplementary Material 2). Pressure and temperature conditions responsible for the macrocrystic assemblage have been calculated using the clinopyroxene-composition barometer of Putirka (2008) and QUILF thermometry (Andersen et al., 1993) respectively. The average pressure calculated for glomerocryst-hosted clinopyroxene crystals (n=36) was 825 ±80 MPa, at a maximum depth of 28 km (assuming a continental crustal density of 2.7 g cm^{-3}). Assuming a higher H_2O content (up to 3.8%; Clocchiatti et al., 1994) yields a slightly lower temperature and pressure, but still within the calculated standard deviation (see Table 7). The average temperature calculated from mean olivine, clinopyroxene and magnetite values was 953°C, with a range of 789-1117°C, owing to the chemical variability in core compositions. Clinopyroxene microcryst compositions have been used in conjunction with literature-sourced shoshonitic and latitic compositions, as well as trachytic compositions from this study, to estimate pressure conditions relating to enclave groundmass crystallisation in a potential shoshonitic-latitic (compositions from De Astis et al., 1997; 2013; Del Moro et al., 1998; Gioncada et al., 1998) and trachytic (from this study) magma (clinopyroxene-liquid barometry; melt barometry of Putirka et al., 2003). SOLVCALC thermometry (Wen and Nekvasil, 1994) has been used to estimate trachytic groundmass temperature conditions using plagioclase and alkali feldspar microlite enclave groundmass compositions. Pressure and temperature calculations for the crystallisation of the shoshonitic-latitic magma give an average of 707 ±80 MPa, with a temperature range of 1089-1149°C. The trachytic magma has an average pressure of 640 ±74 MPa and temperature range of 1000-1130°C. These calculations give an average depth of shoshonite and trachyte magma at ~23-26 km, at the Moho and just above the estimated storage depth of the macrocryst assemblage. These results are consistent with the model presented by De Astis et al. (2013), with replenishment and mixing of distinct magmas postulated to occur in the lower crust and around the Moho.

Since Rhyolite-MELTS permits more accurate modelling of rhyolitic chemical systems compared to Pele 8.00 and MELTS (Gualda et al., 2012), new data and thermometric calculations

allow for a reassessment of rhyolite magma liquidus temperatures, and the interaction between the glomerocryst-bearing enclave magma and the rhyolitic host prior to eruption. Previous fluid inclusion studies (Clocchiatti et al., 1994) reveal the rhyolitic magma host to be in thermal equilibrium with quartz-rich xenoliths, at 30-60 MPa. Barometrical (Zanon et al., 2003; Frezzotti et al., 2004) and petrological data (De Astis et al., 1997) constrain the shallower magma ponding system to depths of 3-4 km. A shallower magma ponding system has been inferred beneath the Fossa Cone by Clocchiatti et al. (1994), at a depth of ~2 km (Clocchiatti et al., 1994). The average liquidus temperature bracket calculated here for the rhyolitic magma is 953-979°C (Rhyolite-MELTS thermometry; Gualda et al., 2012).

Textural observations, geochemistry and thermobarometric calculations made here suggest that up to four magmatic phases interacted at various depths during the evolution of the Pietre Cotte system: (1) A deeper, mafic glomerocryst-forming magma, predominantly containing mafic minerals (clinopyroxene, olivine, magnetite), plagioclase, minor (antecrystic and likely trachyte-derived) alkali feldspar and biotite (the latter identified by Perugini et al., 2007; De Astis et al., 2013); (2) a shoshonitic-latitic magma, identified in several Fossa Cone studies (Keller, 1980; De Astis et al., 1997; 2013; Gioncada et al., 2003; Mandarano et al., 2016; Nicotra et al., 2018); (3) a trachytic enclave composition, identified here by groundmass glass compositions (also identified in Pietre Cotte enclaves by Keller, 1980; Piochi et al., 2009; Vetere et al., 2015; Nicotra et al., 2018), containing alkali feldspar and plagioclase microlites, less common clinopyroxene microcrysts, interstitial glass, large resorbed and prismatic euhedral plagioclase and glomerocrysts; (4) a rhyolitic host magma, containing enclaves of variable compositions (from basaltic-shoshonitic to more typical latitic and trachytic) and enclave-derived antecrysts. The shoshonitic magma contains a mineral assemblage of clinopyroxene (Mg# 0.72-0.89), olivine (Fo_{49-66}), magnetite (Usp_{7-26}), plagioclase (An_{40-63}), apatite and alkali feldspar (Or_{41-57}). Biotite has also been previously identified (Perugini et al., 2007; De Astis et al., 2013). Enclaves contain plagioclase (An_{43-47}) and alkali feldspar (Or_{33-57}) microlites, clinopyroxene (Mg# 0.75-0.81) microcrysts and glomerocrysts of the shoshonitic mineral assemblage. The rhyolitic host contains enclave-derived macrocrysts and glomerocrysts.

5.2. Magma interactions at lower crustal depths

Whole rock enclave compositions, typically from smaller (<20 cm in diameter) enclaves containing abundant glomerocrysts, show an average composition of shoshonite, with interstitial groundmass glass showing a latitic-trachytic composition. These results are consistent with the broad range of reported Fossa Caldera compositions from shoshonitic up to rhyolitic, and extend the range of

compositions for Pietre Cotte beyond the latitic-trachytic range. Overall variations in SiO_2 in the Fossa suite may be attributed to AFC processes (De Astis et al., 2013). Such AFC processes can also lead to the enrichment of K_2O and incompatible elements (Del Moro et al., 1998; Francalanci et al., 2007; Mandarano et al., 2016). A more deeply-sourced (18.5-21 km) basaltic-shoshonitic magma has previously been suggested to be present below the Fossa Cone (Nicotra et al., 2018). Given the range of observed Pietre Cotte enclave and Fossa magma compositions more generally, the shoshonitic and trachytic enclave compositions identified in this study are considered to represent distinct components of the Pietre Cotte magmatic system; reported shoshonitic, latitic and lati-trachytic compositions may represent intermediate compositions of variable glomerocryst abundance and degree of magma differentiation between the two magma-types. These compositions may reflect end-members stored at various depths below the Fossa Cone, specifically a deeper, shoshonitic magma (responsible for the macrocryst-glomerocryst assemblage), and progressively shallower shoshonitic, latitic and trachytic enclave magmas that carry the macrocryst assemblage.

Petrographic observations and glass geochemistry suggest that a mafic crystal cumulate resides at depth (up to 28 km) below the Fossa Cone. This cumulate is represented by glomerocrysts within the enclave magma and rhyolitic host, comprised of clinopyroxene, olivine, magnetite, plagioclase, minor alkali feldspar and biotite. Observations made in this study indicate that the macrocryst assemblage is not in equilibrium with the enclave magma in which it predominantly occurs. Injection of a new input of magma from depth may disrupt and mobilise a crystal mush, resulting in glomerocrysts in the enclave magma. Due to the inherited heterogeneity and disequilibrium effects from interacting phases, the bulk rock analysis of enclaves represents the average content of two mingled compositions rather than the enclave parental magma composition. Therefore, mineral chemistry and textural relationships offer greater insights into the magmatic evolution of the glomerocrysts and the enclave magma. Thermometric calculations highlight a wide temperature range in cumulate formation (789-1117°C), which may reflect a differential cooling regime at depth and possible interactions with a hotter proximal magma. This applied heating may come from shoshonitic-latitic magmas, considered to reside at similar or slightly shallower depths (18-21 km, Zanon et al., 2003; Peccerillo et al. 2006; Fusillo et al., 2015; Nicotra et al., 2018; up to 30 km depth; Petrelli et al., 2018), or by input from more mafic and hotter recharge events. New inputs of magma are likely to occur as the Fossa plumbing system has been characterised by many small magma batches interacting (Clocchiatti et al., 1994; Del Moro et al., 1998; Zanon et al., 2004; Piochi et al., 2009; De Astis et al., 1997; 2013). Clinopyroxene exhibits chemical zonation, formed by changes in composition or temperature of the magmatic system, and an increasing Mg# towards the

rim, both of which may reflect magma replenishment. The suggestion of a refilling process is also supported by the enrichment of alkali elements, as suggested by Del Moro et al. (1998). The increasing An content and Mg# towards the edges of glomerocryst-derived plagioclase and clinopyroxene phases respectively also supports a later mafic refilling. Glomerocrysts and cumulate lithologies in similar systems have been previously attributed to mafic recharge, providing sufficient heat to remobilise crystal mush material, resulting in the coexistence of crystal-rich enclaves of texturally and compositionally disequilibrated mineral phases. This process of rejuvenation has been identified in many felsic magmatic systems (Bachmann et al., 2002; Bachmann and Bergantz, 2003, 2004, 2006; Shane et al., 2005; Forni et al., 2015; Wolff et al., 2015).

De Astis et al. (2013) described plagioclase, alkali feldspar and biotite as the generally prevalent phenocryst assemblage in trachytes of Vulcano, while shoshonitic-latitic rocks display mineral assemblages consisting of plagioclase, clinopyroxene, magnetite and olivine. The glomerocryst mineral assemblage (Fig. 4) is typically associated with Vulcano shoshonitic to latitic compositions (De Astis et al., 2013), potentially evolved from a crystal mush. Glomerocryst-derived clinopyroxene compositions are more closely equilibrated with shoshonitic compositions (followed by latitic compositions) than the trachytic melt with which they are in contact (Fig. 13; clinopyroxene equilibria test of Putirka, 2008). These results indicate that clinopyroxene began to crystallise in a more primitive magma than a latite. Evidence suggests that the glomerocrysts may have been formed by melting of lower temperature phases such as alkali feldspar (note that resorption is evident in the samples; Fig. 5d) and biotite (rarely evident in glomerocrysts), reducing the crystallinity and remobilising the cumulate. The scarcity of alkali feldspar and biotite may therefore be due to their melting at high temperatures. Plagioclase crystals show enrichment in Ab towards the rim, and abundant alkali feldspar is more abundant in the trachytic enclave groundmass. Therefore, the trachytic magma may have derived from cumulate melting plus mixing with a mafic recharge magma. This would result in compositional variations in magmas near the Moho, including the mafic cumulate (up to 28 km depth), shoshonitic to latitic magmas (up to 26 km depth at 1089-1149°C) fed from deeper mafic inputs, and a trachytic magma (up to 23 km depth, 1000-1130°C).

Cumulates may be mobilised by fresh mafic inputs, and the resulting glomerocrysts represent the refractory residue of the cumulate dissolution and/or partial melting, after interaction with the recharge magma. As well as the clear size contrast between the macrocryst glomerocrysts and the microlitic trachytic groundmass as a whole, there is also a more subtle contrast within the trachytic groundmass. There are patches of slightly coarser-grained groundmass material (compared to other areas of groundmass) within trachytic enclaves, often coinciding with resorbed and zoned macrocrysts and glomerocrysts (Fig. 5). Interaction between marginally hotter cumulate assemblage

and cooler trachytic magma may have promoted a slight prolonged cooling history, promoting coarsening of the trachytic groundmass in the immediate vicinity to the glomerocrysts. As trachytic compositions do not consistently plot between the shoshonitic and rhyolitic compositions (Fig. 9), it can be assumed that the trachytic magma is not the product of mixing between mafic and rhyolitic Fossa Cone magma compositions. However, this assumption is tentative as different elements have different diffusion mobilities (e.g. in a time-series of high temperature experiments, Na has been shown to have a higher mobility than K and other major elements, while Rb, Sr and Ba have high diffusivities compared to the REEs, Nb, Ta, Zr, and Hf; Perugini et al., 2015). The inherent complexity of mixing systems results from the interplay of fluid dynamic regimes and chemical exchanges between interacting magmas (Rossi et al., 2017). While examples of data such as that shown in Fig. 9 can indicate system variability between two end-members, this may still be skewed with variations in chaotic mixing processes such as duration of mixing time, degree of crystallinity and the role of volatiles dissolved in a melt (Rossi et al., 2017).

5.3. Magma ascent through the middle crust

Continuous depletions in MgO, Fe_2O_3, TiO_2 and CaO with increasing SiO_2 contents (Fig. 9) represent clinopyroxene, olivine and magnetite fractionation from mafic compositions. The notable negative P anomaly (Fig. 8) and bulk-rock P_2O_5 decrease from intermediate compositions (Fig. 9), indicate fractionation of accessory apatite from the intermediate magma. The peaked trends and observed variations of Al_2O_3, K_2O and Sr with increasing SiO_2 content (Figs. 9-10) indicates two-feldspar fractionation occurred from intermediate to rhyolitic compositions. Observed CaO variations have been previously attributed to accumulations of plagioclase phenocrysts and/or xenocrysts (Nicotra et al., 2018). Europium and Ba depletion in the rhyolitic host (Fig. 8) also suggests substantial removal of two feldspars, with Ba associated with alkali feldspar fractionation, and Al_2O_3, Ba, Sr and Eu associated with plagioclase fractionation. The Eu anomaly is attributed to plagioclase fractionation at low oxygen fugacity (fO_2) conditions, although it may also be the product of assimilation or partial melting of crustal material, as a negative Eu anomaly is also a feature of post-Archean upper continental sediments (Taylor and McLennan, 1985; Rudnick, 1992). Observed trends in Zr and Nb with increasing SiO_2 (peaking and decreasing at rhyolitic compositions) suggests late zircon fractionation as an accessory phase, previously identified in other Vulcanello and Fossa Cone products (De Astis et al., 2013).

As the trachyte evolves, plagioclase (with increasing An towards the rim) and eventually alkali feldspar grow as phenocrysts and later (i.e., at shallower depths) as the microlitic groundmass.

Plagioclase forms individually, or nucleates upon mafic glomerocrysts. Microlitic plagioclase and alkali feldspar laths are intergrown, suggesting that these crystals grew simultaneously. The scarcity of phenocrysts and the presence of trachytic groundmass glass in enclaves suggests that the ascent of the trachyte towards the upper crust was relatively rapid, suppressing crystal growth. Plagioclase is assumed to either crystallise below the lower clinopyroxene and olivine crystallisation limit, or at a faster growth rate. This is because plagioclase crystals often engulf smaller clinopyroxene and olivine crystals. The presence of large (up to 1.5 mm), resorbed plagioclase crystals with slightly higher An content, distinct in appearance from more pristine and generally smaller (lower An) plagioclase crystals, suggests a separate origin. The plagioclase equilibrium test (cf. Putirka, 2008) suggests disequilibrium between the plagioclase rims and the rhyolitic melt, but equilibrium is achieved for plagioclase rims and the trachytic glass (observed output values of 0.06-0.09 for four tests), at temperatures below 1,050°C, consistent with the lower range trachyte temperature calculations. Larger, resorbed plagioclase crystals may represent antecrysts which mingled with the ascending trachyte in mid-crustal levels (between deeper, mafic parental magmas near the Moho, and the shallower rhyolite below the Fossa Cone). Several magma reservoirs have been inferred at these depths by De Astis et al. (2013) and Nicotra et al. (2018), which were active over the last 1000 years, producing shoshonitic to trachytic compositions. Nicotra et al. (2018) computed a plagioclase nucleation and residence at ~11 km of depth by MELTS simulations, and suggested mingling with latitic and trachytic magmas at 3.6–5.5 km depth. A shallow, rigid mush is also suggested, accounting for the short timescales of ascent (~2-10 years) compared to the eruption recurrence (decades to hundreds of years), whereby low temperatures and high viscosity preclude the magmatic convection capability (Cooper and Kent, 2014; Nicotra et al., 2018).

The presence of a shallow (mid-crustal), plagioclase-rich crystal mush may have also generated the rhyolitic magma, with the evolved melt separated from the cumulate by melt extraction and AFC at shallow (mid- to upper crustal) depths, just below the rhyolite storage depth. The pronounced negative Eu anomaly indicates feldspar-liquid separation, supporting this method of rhyolite generation. It has also previously been suggested that Fossa Cone rhyolitic compositions formed by AFC processes from a more primitive mafic magma (De Astis et al., 1997, 2013; Gioncada et al., 1998; Frezzotti et al., 2004; Piochi et al., 2009). Results from trace element modelling and AFC calculations provide an indication of how the rhyolitic magma formed, though inherent complexities of this dynamic system mean that limitations in the AFC modelling should be considered (Perugini et al., 2015; Rossi et al., 2017). Trace element modelling shows that rhyolitic host compositions can be generated by AFC processes at rates of 0.2 (fractionation-dominated processes) to 0.5 assimilation vs. fractionation (r value; Fig. 11). A shoshonitic bulk rock trace element content from this study was

selected as a starting composition. The positive correlation of Yb with Zr and the negative correlation of Sr with Nb, Sr with Zr can be successfully modelled by AFC processes (using a Calabro-Peloritano basement assimilant, Frezzotti et al., 2004; parameters shown in Supplementary Material 2), especially if moderate rates of assimilation are assumed (r value = 0.2 to 0.5). Trace element modelling suggests that the rhyolitic host evolved from a magma similar to the shoshonitic Fossa Cone compositions measured in previous work (De Astis et al., 1997; Del Moro et al., 1998) and in this study, and assimilated crustal material. Previous Pietre Cotte isotopic studies, which assume a starting composition of isotopically similar Etna mafic rocks (DePaolo, 1981; Ellam et al., 1988; De Astis et al., 1997, 2013; Del Moro et al., 1998; Gioncada et al., 1998; Piochi et al., 2009), have also shown that the rhyolite can be produced by AFC processes from a mafic parental magma. The model of less differentiated products of Vulcano by Del Moro et al. (1998) indicates that FC may have generated some of the Pietre Cotte latitic and trachytic products, while AFC is responsible for the evolution from trachytic to rhyolitic magma compositions. It is possible that FC conditions prevailed in the early evolution of latitic and eventual trachytic magmas, with AFC processes only occurring in the shallow crust.

5.4. Shallow crustal-level interactions

Cuspate, crenulated and lobate contacts at the enclave edge (Figs. 2-3, 6) signify that one magma was cooler and more viscous than the other when they came in contact with each other. The presence of chilled margins and vesiculation at the trachytic enclave-rhyolite host interface (Fig. 4) indicate a temperature contrast may have locally dissolved the rhyolitic material, and with some potential hybridisation at the enclave edge (Eichelberger, 1980). Vesicles at the rim may have been caused by heating of the surrounding rhyolite, and consequent cooling of the trachytic enclave, causing exsolution of volatile components and vesiculation at enclave edges. This may also result in an increased buoyancy of enclaves (Cardoso and Woods, 1999), resulting in the ascent, mingling and larger spatial distribution of enclaves in the host, as seen in outcrop. There are also some angular enclaves evident in the host lava, suggesting that at least some of the trachytic magma was already solidified during these interactions. Rapid quenching would be responsible for the development of the microlitic groundmass of the enclaves (Giordano et al., 2004; Morgavi et al., 2016). Rapid crystallisation of the microlitic enclave groundmass may have markedly increased the magma viscosity, affecting rheology and inducing a more rigid behaviour. Perugini and Poli (2005, 2011) suggested that the invasion and displacement of a more mafic, less viscous magma into a more viscous rhyolitic magma led to an instability and viscous finger formation at the contacts between

the two magmas. The enclave magma viscosity has been previously calculated as $10^{4.8} \leq \eta \leq 10^{5.0}$ Pa s, and the rhyolitic magma viscosity as $10^{5.11} \leq \eta \leq 10^{5.6}$ Pa s (Vetere et al., 2015). An injection such as this can also trigger local convection and fragmentation (Perugini et al., 2007; Vetere et al., 2015), resulting in the brittle separation of fingers. Perugini et al. (2007) suggested that fragmented and cuspate enclaves result from fragmentation of viscous fingering structures during replenishment of the rhyolitic magma by the enclave magma prior to eruption.

The enclave magma could have been in a solid or semi-solid state during interaction with the rhyolite, such that significant mixing, elongation or band formation during mingling, ascent, eruption and emplacement, would have been inhibited. The identification of more rigid enclaves here and in other studies (Perugini et al., 2007; Piochi et al., 2009; Vetere et al., 2015) signifies that the enclave magma may have been near solidification temperature during interaction, and variable cooling may have led to solidification of some enclaves. Minor fragmentation may then have led to the development of more rigid, angular enclaves. Vetere et al. (2015) point to the fact that enclaves are dispersed in the rhyolitic host as isolated fragments, suggesting limited collision and fragmentation during flowing of the magma and eruption (see also Perugini et al., 2007). The separation of glomerocrysts and coarse macrocrysts from the enclave into the rhyolitic host indicates that, when this occurred, the two interacting phases may have been semi-molten and malleable but also show some tensile strength, as separated glomerocrysts and minerals surrounded by a thin film of enclave groundmass are typically rounded (by resorption, convection, ascent and/or flow emplacement), but not stretched out or sheared.

The rhyolitic host contains sparse-to-widespread microlites and spherulites. Spherulite nucleation at the edge of enclaves (Fig. 3a) and wrapping enclaves suggests semi-solid rheological behaviour. Spherulite nucleation may have had an early onset, based on microlite deflections around spherulites (Bullock et al., 2017). However, spherulite formation is predominantly a subsolidus process (Clay et al., 2013; Befus et al., 2015; Bullock et al., 2017) in the Pietre Cotte rhyolitic host, and the majority of spherulites overprint microlites (Bullock et al., 2017). Therefore, the presence of spherulites nucleating upon enclaves suggests that enclaves were at least semi-solid whilst interacting with the rhyolite host. Further spherulite nucleation (overprinting microlites, wrapping enclaves) occurred as a down-temperature continuous process in the subsolidus (Bullock et al., 2017). This interpretation is further supported by the presence of vesicles around enclaves, which suggests solid state rheological behaviour of enclaves (Blake and Fink, 2000; Vetere et al., 2015). Reported water values of <0.08 wt% in the rhyolite (Piochi et al., 2009) are consistent with an early volatile loss from the system and/or shallow crystallisation. Microlite crystallisation in the Pietre Cotte rhyolitic host may have occurred as a response to decompression-induced magma

degassing (Hammer and Rutherford 2002; Couch et al., 2003; Blundy and Cashman 2005; Mollard et al., 2012; Preece et al., 2016). As transfer of the macrocryst mafic assemblage from the trachytic enclaves to the rhyolitic host has been observed, it is also plausible that microlites may also have transferred during magma mingling (see also Martel et al., 2006; Humphreys et al., 2009). This would require high shear stress, which can occur during ascent through the conduit or upon extrusion and during flow-related deformation.

5.5. Texture-forming processes in the Fossa Cone magmatic system

A basaltic-shoshonitic magma has been previously considered to reside at depth in the lower crust, feeding the shallow magma reservoir of both the Fossa Cone and the neighbouring Vulcanello crater, which may trigger eruptions following migration from depth (Gioncada et al., 1998; Zanon et al., 2003; De Astis et al., 2013; Fusillo et al., 2015; Nicotra et al., 2018). Zanon et al. (2003) showed evidence for deep magma storage for the Vulcanello eruptive products of 18-21 km, close to the Moho, and it has been suggested that this could be the same for a basaltic magma at depth below the Fossa Cone (Nicotra et al.; 2018). Based on textural and micro-compositional data on plagioclase crystals from recent (<1000 year old) eruptive products, Nicotra et al. (2018) identified three magma storage levels between 2 and 17 km depth beneath the Fossa Cone. Plagioclase textural and compositional data preserve evidence for regular activity over the last 1000 years, demonstrated by records of ascent and continuous episodes of magma recharge and mixing affecting the shallower Fossa reservoirs (Nicotra et al., 2018). The ascent of a shoshonitic magma from depth followed by recharge and mixing episodes has previously been suggested as an eruption trigger at the Fossa Cone (Nicotra et al., 2018). Shoshonitic compositions that extrude at the surface at the neighbouring Vulcanello edifice may represent a magma that ascended from depth, directly reaching the surface without any prolonged storage, mixing/mingling or evolution at mid-crustal levels. Latites at shallow- to mid-crustal depths may represent an almost pure end-member composition (up to trachytic compositions with intermediate lati-trachytic compositions) which rose directly up during the last 1000 years of activity (Nicotra et al., 2018).

A mid-crustal magma storage depth between 12.5 and 16.8 km has been proposed by De Astis et al. (2013) and Fusillo et al. (2015), supported by textural studies of plagioclase crystals by Nicotra et al. (2018), represented by a shoshonitic to latitic composition at ~11 km depth. A latitic magma is also suggested for the source of crater fumarolic field gases from a shallow (<40 MPa) latitic ponding level via a degassing path at the Fossa Cone (Paonita et al., 2013), and a latitic-trachytic reservoir is further proposed at depths of 3.6–5.5 km (Nicotra et al., 2018). The latitic

reservoir is suggested to reside at ~3 km depth, compared to a proposed 1-2 km depth of the rhyolite reservoir (Peccerillo et al., 2006; Paonita et al., 2013). Fluids and melts may have been supplied to the latitic magma from an underlying reservoir with a mafic character (Paonita et al., 2013).

Based on the combined thermobarometric calculations, textural observations, geochemical data presented here and a synthesis of the literature data, we propose a model of magmatic evolution leading to the extrusion of the Pietre Cotte lava flow of seven stages, as follows (and illustrated in Fig. 15):

1. Mobilisation of a mafic crystal mush (at temperatures up to ~1150°C and depths of up to 28 km) by magma replenishment, resulting in glomerocryst formation (made up of macrocrystic clinopyroxene, olivine, magnetite, plagioclase, rare antecrystic alkali feldspar, biotite and apatite) in a shoshonitic-latitic magma.
2. Fractional crystallisation of shoshonitic-latitic magma to a trachytic magma (between ~16 and 24 km, ~1000-1130°C) and ascent through the lower crust, with crystallisation of plagioclase, alkali feldspar and clinopyroxene.
3. Ascent through the upper crust and microlite crystallisation, with incorporation of large (up to 15 mm) plagioclase xenocrysts at ~11 km depth (Nicotra et al., 2018).
4. Rhyolite storage in a small volume reservoir at shallower (60 MPa and <5 km) depths and lower liquidus temperatures (940-965°C).
5. Mingling of glomerocryst-bearing trachytic magma with rhyolitic magma.
6. Rapid ascent of enclave-bearing rhyolitic magma through conduit with microlite and spherulite nucleation in the rhyolite.
7. Extrusion of the Pietre Cotte lava flow, followed by flow-related deformation, further spherulite nucleation and vapour-phase crystallisation.

The likely interaction between several connected reservoirs of variable compositions at numerous depths beneath the Fossa Cone down to the lower crust (Clocchiatti et al., 1994; Paonita et al., 2002; 2013; Zanon et al., 2003; Peccerillo et al., 2006; Piochi et al., 2009; De Astis et al., 2013; Mandarano et al., 2016; Nicotra et al., 2018) means that enclaves may span a range of compositions from shoshonite-latite to trachyte (Piochi et al., 2009; De Astis et al., 1997; 2013; Nicotra et al., 2018; this study). The whole rock enclave composition is dependent upon degree of differentiation, mixing and interaction between magmas, and abundance of glomerocrysts within a given enclave.

While a deeper basaltic-shoshonitic magma may reside at lower crustal depths for decades to hundreds of years (Nicotra et al., 2018), the ascent and mingling of the deeper mafic magma with

the shallower rhyolite would plausibly have triggered ascent and eruption on a more rapid timescale. Short residence times for magmas stored at shallower depths have previously been suggested for recent Fossa Cone eruptive products by Zanon et al. (2003) and Nicotra et al. (2018). Diffusion modelling of Sr zoning within plagioclase suggest residence times of 2-10 years for crystals erupted at the Fossa Cone, compared to 2–3 years calculated residence times for crystals of the 1888–90 eruption and <2 years for Vulcanello eruptions (Nicotra et al., 2018).

The identification of these magmatic processes occurring at various depths is important for volcano monitoring and hazard assessment in active areas such as Vulcano. A volcanic chronometry study of Perugini et al. (2015) found that water-rich melt systems may migrate towards the surface on timescales in the order of hours to days, potentially triggering explosive eruptions with short warning times and devoid of long-term geophysical precursors (see also Cashman, 2013; Edmonds and Wallace, 2017; Petrelli et al., 2018). Therefore, the role of high-resolution petrological investigations in geophysical and volcanological research can aid our understanding of mingling and cumulate remobilisation at depth, potentially providing longer warning times for eruption forecasting (Petrelli et al., 2018).

6. Conclusions

Petrographic observations, whole rock major and trace element geochemistry and mineral chemistry indicate that there were up to four compositions interacting during the evolution of the Pietre Cotte magmatic system: (1) a shoshonitic crystal mush, resulting in a predominantly mafic, macrocrystic assemblage, that dominantly manifests as glomerocrysts, (2) a shoshonitic-latitic magma, (3) a microlitic-to-microcrystic trachytic enclave magma, which hosts the glomerocrysts and (4) a glassy rhyolitic magma, which hosts enclaves, enclave-derived macrocrysts and glomerocrysts. The crystal mush remobilised and interacted with the shoshonitic to latitic-trachytic magmas at similar depths, before ascent and mingling of the trachyte with a shallower rhyolitic host. Crystal mush remobilisation accounted for the coexistence of texturally and compositionally disequilibrated mineral phases within trachytic enclaves and eventually the rhyolitic host. This study contributes new data and interpretations to the problem of how the primary magmas associated with the Pietre Cotte lava flow evolved and how glomerocrysts were formed in the enclave magma and rhyolitic host. The findings of this study also emphasise the importance of furthering our understanding of texture-forming conditions associated with multiple magmatic events that occur on short timescales, exemplified in this active Lipari-Vulcano Aeolian Island setting.

Acknowledgments

The authors wish to gratefully acknowledge Andy Tindle (The Open University) for assistance with EMP analyses. LB acknowledges support from Keele University, and grants from the Geologists' Association, Mineralogical Society (UK and Ireland) and Volcanic and Magmatic Studies Group for fieldwork and whole rock analysis. LAB is grateful to Sophie Blanchard for assistance with MATLAB. The authors are grateful for the thorough and constructive comments from Francesca Forni and two anonymous reviewers, as well as the careful editorial handling of Alessandro Aiuppa, which greatly improved this manuscript.

Highlights:

- Disequilibrium textures in the Pietre Cotte lava flow signify a complex evolution
- Petrography and geochemistry highlight several magmatic mingling events
- Crystal mush, trachyte and rhyolite magmas interacted at various crustal depths
- Shallow magmatic interactions may trigger eruptions following migration from depth

References

Albarede F (1995) Introduction to Geochemical Modelling 543 pp, Cambridge Univ. Press, New York.

Andersen D, Lindsley DH, Davidson PM (1993) QUILF: A pascal program to assess equilibria among Fe-Mg-Mn-Ti oxides, pyroxenes, olivine, and quartz. Comput Geosci 19(9), 1333-1350.

Anderson AT (1976) Magma mixing: petrological process and volcanological tool. J Volcanol Geoth Res 1:3–33.

Arrighi S, Tanguy J, Rosi M, (2006) Eruptions of the last 2200 years at Vulcano and Vulcanello (Aeolian Islands, Italy) dated by high-accuracy archeomagnetism. Phys Earth Planet Inter 159:225-233.

Asimow PD, Ghiorso MS (1998) Algorithmic Modifications Extending MELTS to Calculate Subsolidus Phase Relations. Am Mineral 83:1127–1131.

Bachmann O, Bergantz GW (2003) Rejuvenation of the Fish Canyon magma body: a window into the evolution of large-volume silicic magma systems. Geology 31:789-792.

Bachmann O, Bergantz GW (2004) On the origin of crystal-poor rhyolites: extracted from batholithic crystal mushes. J Petrol 45, 8:1565–1582.

Bachmann O, Bergantz GW (2006) Gas percolation in upper-crustal silicic crystal mushes as a mechanism for upward heat advection and rejuvenation of near-solidus magma bodies. J Volcanol Geoth Res 149:85–102.

Bachmann O, Dungan MA, Lipman PW (2002) The Fish Canyon magma body, San Juan volcanic field, Colorado: rejuvenation and eruption of an upper-crustal batholith. J Petrol 43:1469–1503.

Bacon CR, Sisson TW, Mazdab FK (2007) Young cumulate complex beneath Veniaminof caldera, Aleutian arc, dated by zircon in erupted plutonic blocks. Geology 35(6):491–494.

Baier J, Audétat A, Keppler H (2008) The origin of the negative niobium tantalum anomaly in subduction zone magmas. Earth Planet Sci Lett 267(1-2):290–300.

Barker AK, Troll VR, Carracedo JC, Nicholls PA (2015) The magma plumbing system for the 1971 Teneguía eruption on La Palma, Canary Islands. Contrib Mineral Petrol 170(54):1-21.

Befus KS, Watkins J, Gardner JE, Richard D, Befus KM, Miller NR, Dingwell DB (2015) Spherulites as in-situ recorders of thermal history in lava flows. Geology 43:647-650.

Blake S, Fink JH (2000) On the deformation and freezing of enclaves during magma mixing. J Volcanol Geotherm Res 95:1–8.

Blundy JD, Cashman K (2005) Rapid decompression-driven crystallization recorded by melt inclusions from Mount St Helens volcano. Geology 33 (10), 10.2005:793–796.

Boudreau AE (1999) PELE—a version of the MELTS software program for the PC platform. Comput Geosci 25:21–203.

Bullock LA, Gertisser R, O'Driscoll B (2017) Spherulite formation in obsidian lavas in the Aeolian Islands, Italy. Period Mineral 86:37–54.

Cardoso SSS, Woods AW (1999) On convection in a volatile-saturated magma, Earth Planet Sci Lett 168:301-310.

Clay PL, O'Driscoll B, Gertisser R, Busemann H, Sherlock SC, Kelley SP (2013) Textural characterization, major and volatile element quantification and Ar–Ar systematics of spherulites in the Rocche Rosse obsidian flow, Lipari, Aeolian Islands: a temperature continuum growth model. Contrib Mineral Petrol 165(2):373-395.

Clocchiatti R, Del Moro A, Gioncada A, Joron JL, Mosbah M, Pinarelli L, Sbrana A (1994) Assessment of a shallow magmatic system: the 1888–90 eruption, Vulcano Island, Italy. Bull Volcanol 56:466–486.

Couch S, Sparks RSJ, Carroll MR (2003) The kinetics of degassing-induced crystallization at Soufrière Hills Volcano, Montserrat. J Petrol 44:1477–1502.

Dahren B, Troll, VR, Andersson UB, Chadwick JP, Gardner MF, Jaxybulatov K, Koulakov I (2012) Magma plumbing beneath Anak Krakatau volcano, Indonesia: evidence for multiple magma storage regions. Contrib Mineral Petrol 163(4):631-651.

Davì M (2007) The Rocche Rosse rhyolitic lava flow (Lipari, Aeolian Islands): magmatological and volcanological aspects. Plinius 33:1-7.

Davì M, De Rosa R, Barca D (2009) A LA-ICP-MS study of minerals in the Rocche Rosse magmatic enclaves: Evidence of a mafic input triggering the latest silicic eruption of Lipari Island (Aeolian Arc, Italy). J Volcanol Geotherm Res 182:45-56.

Davì M, De Rosa R, Donato P, Sulpizio R (2011) The Lami pyroclastic succession (Lipari, Aeolian Islands): a clue for unravelling the eruptive dynamics of the Monte Pilato rhyolitic pumice cone. J Volcanol Geotherm Res 201:285–300.

De Astis G, La Volpe L, Peccerillo A, Civetta L (1997) Volcanological and petrological evolution of Vulcano island (Aeolian Arc, southern Tyrrhenian Sea). J Geophys Res 102:8021–8050.

De Astis G, Lucchi F, Dellino P, La Volpe L, Tranne CA, Frezzotti ML Peccerillo A (2013) Geology, volcanic history and petrology of Vulcano (central Aeolian archipelago). In: Lucchi F, Peccerillo A, Keller J, Tranne CA, Rossi PL (eds) The Aeolian Islands Volcanoes. Geological Society, London, Memoirs, 37:281–349.

De Fiore O (1922) Vulcano (Isole Eolie). Monografia – Zeitschrift fur Vulkanologie 3, 3–393. (Rep. Swets and Zeitlinger N. V., Amsterdam, 1969).

Del Moro A, Gioncada A, Pinarelli L, Sbrana A, Joron JL (1998) Sr, Nd, and Pb isotope evidence for open system evolution at Vulcano, Aeolian Arc, Italy. Lithos 43:81–106.

Dellino P, De Astis G (2008) Relazione scientifica per la predisposizione del piano di emergenza vulcanica all'isola di Vulcano. INGV-DPC Projects 2005–2007, Final report on Project V3_5 – Vulcano:1–64.

Dellino P, La Volpe L (1997) Fragmentation versus transportation mechanism in the pyroclastic sequence of Monte Pilato-Rocche Rosse (Lipari, Italy). J Volcanol Geoth Res 64:211–231.

DePaolo DJ (1981) Trace element and isotopic effects of combined wall-rock assimilation and fractional crystallization. Earth Planet Sci Lett 53, 189–202.

Di Traglia F (2011) The last 1000 years of eruptive activity at the Fossa Cone (Island of Vulcano, Southern Italy). PhD thesis, Università degli Studi di Pisa, Italy.

Eichelberger JC (1980) Vesiculation of mafic magma during replenishment of silicic magma reservoirs. Nature 288:446-450.

Ellam RM, Menzies MA, Hawkesworth CJ, Leeman WP, Rosi M, Serri G (1988) The transition from calc-alkaline to potassic orogenic magmatism in the Aeolian Islands, southern Italy. Bull Volcanol 50:386–398.

Ersoy Y, Helvaci C (2010) FC–AFC–FCA and mixing modeler: A Microsoft® Excel© spreadsheet program for modeling geochemical differentiation of magma by crystal fractionation, crustal assimilation and mixing. Comput Geosci 36(3):383–390.

Falsaperla S, Neri G, Velardita S (1985) Struttura della crosta superiore dell'area delle isole Eolie. Rend Osserv Geofis Reggino 29, 103-111.

Ferreira T, Rasband W (2012) ImageJ User Guide IJ 1.46r. Available online: https://imagej.nih.gov/ij/docs/guide/user-guide.pdf (Accessed 08/2017).

Forni F, Ellis BS, Bachmann O, Lucchi F, Tranne CA, Agostini S, Dallai L (2015) Erupted cumulate fragments in rhyolites from Lipari (Aeolian Islands). Contrib Mineral Petrol 170, 49.

Fourcade S, Allegre CJ (1981) Trace element behaviour in granite genesis: a case study the calc-alkaline plutonic association from the Querigut Complex (Pyrenees France). Contrib Mineral Petrol 76:177–195.

Francalanci L, Avanzinelli R, Tommasini S, Heuman A (2007) A west–east geochemical and isotopic traverse along the volcanism of the Aeolian Island arc, southern Tyrrhenian Sea, Italy: inferences on mantle source processes. In: Beccaluva L, Bianchini G, Wilson M (eds) Cenozoic Volcanism in the Mediterranean Area. Geological Society of America, Denver, USA, pp.235–263.

Frazzetta G, La Volpe L, Sheridan MF (1984) Evolution of the Fossa cone, Vulcano. J Volcanol Geoth Res 17:329–360.

Frezzotti ML, Peccerillo A, Zanon V, Nikogosian I (2004) Silica-rich Melts in Quartz Xenoliths from Vulcano Island and their Bearing on Processes of Crustal Anatexis and Crust–Magma Interaction beneath the Aeolian Arc, Southern Italy. J Petrol 45:3–26.

Frost BR, Lindsley DH (1992) Equilibria among Fe-Ti oxides, pyroxenes, olivine, and quartz: Part II Application. Am Mineral 77, 1004- 1020.

Frost BR, Lindsley DH, Andersen DJ (1988) Fe–Ti oxide–silicate equilibria: assemblages with fayalitic olivine. Am Mineral 73, 727–740.

Geist D, Howard KA, Larson P (1995) The generation of oceanic rhyolites by crystal fractionation: the basalt–rhyolite association at Volcan Alcedo, Galápagos Archipelago. J Petrol 36:965–982.

Ghiorso MS, Sack RO (1995) Chemical Mass Transfer in Magmatic Processes. IV. A Revised and Internally Consistent Thermodynamic Model for the Interpolation and Extrapolation of Liquid-Solid Equilibria in Magmatic Systems at Elevated Temperatures and Pressures. Contrib Mineral Petrol 119:197–212.

Gioncada A, Clocchiatti R, Sbrana A, Bottazzi P, Massare D, Ottolini L (1998) A study of melt inclusions at Vulcano (Aeolian Islands, Italy): insights on the primitive magmas and on the volcanic feeding system. Bull Volcanol 60:286–306.

Giordano D, Romano C, Papale P, Dingwell DB (2004) The viscosity of trachytes, and comparison with basalts, phonolites, and rhyolites. Chem Geol 213(1):49–61.

Gualda GAR, Ghiorso MS, Lemons RV, Carley TL (2012) Rhyolite-MELTS: A modified calibration of MELTS optimized for silica-rich, fluid-bearing magmatic systems. J Petrol DOI:10.1093/petrology/egr080.

Hammer JE, Rutherford MJ (2002) An experimental study of the kinetics of decompression-induced crystallization in silicic melts. J Geophys Res 107:ECV8-1–ECV8-24.

Higgins MD (2000) Measurement of Crystal size distributions. Am Mineral 85:1105-1116.

Higgins MD (2002) Closure in crystal size distributions (CSD), verification of CSD calculations, and the significance of CSD fans. Am Mineral 87:171-175.

Higgins MD (2006) Quantitative textural measurements in igneous and metamorphic petrology. 1st edition. Cambridge University Press, Cambridge, 270.

Hildner E, Klügel A, Hauff F (2011) Magma storage and ascent during the 1995 eruption of Fogo, Cape Verde Archipelago. Contrib Mineral Petrol 162:751–772.

Humphreys MCS, Christopher T, Hards V (2009) Microlite transfer by disaggregation of mafic inclusions following magma mixing at Soufrière Hills volcano, Montserrat. Contrib Mineral Petrol 157:609–624.

Jeffery AJ, Gertisser R, Troll VR, Jolis EM, Dahren B, Harris C, Tindle AG, Preece K, O'Driscoll B, Humaida H, Chadwick JP (2013) The pre-eruptive magma plumbing system of the 2007-2008 dome-forming eruption of Kelut volcano, East Java, Indonesia. Contrib Mineral Petrol 166:275–308.

Keller J (1970) Die historischen Eruptionen von Vulcano und Lipari. Zeitschrift Deutsch. Geologie Geochimie, 121:179–185.

Keller J (1980) The island of Vulcano: Società Italiana di Mineralogia e Petrologia 36:368–413.

Launeau P, Bouchez JL, Keith B (1990) Shape preferred orientation of object population: automatic analysis of digitized images. Tectonophysics 180:201–211.

Launeau P, Robin P-YF (1996) Fabric analysis using the intercept method. Tectonophysics 267:91-119.

Le Bas MJ, Lemaitre RW, Streckeisen A, Zanettin B (1986) A Chemical Classification of Volcanic-Rocks Based on the Total Alkali Silica Diagram. J Petrol 27, 3:745–750.

Leeman WP, Hawkesworth CJ (1986) Open magma systems: Trace element and isotopic constraints. J Geophys Res 91:5901-5912.

Leonard G, Cole J, Nairn I, Self S (2002) Basalt triggering of the c. AD 1305 Kaharoa rhyolite eruption, Tarawera Volcanic Complex, New Zealand. J Volcanol Geoth Res 115 (3–4):461–486.

Lindsley DH, Frost BR (1992) Equilibria among Fe-Ti oxides, pyroxenes, olivine, and quartz: Part I. Theory. Am Mineral 77, 987-1003.

Mandarano M, Paonita A, Martelli M, Viccaro M, Nicotra E, Millar IL (2016) Revealing magma degassing below closed-conduit active volcanoes: geochemical features of volcanic rocks versus fumarolic fluids at Vulcano (Aeolian Islands, Italy). Lithos 248-251, 272–287.

Martel C, Radadi Ali A, Poussineau S, Gourgaud A, Pichavant M (2006) Basalt-inherited microlites in silicic magmas: Evidence from Mount Pelée (Martinique, French West Indies). Geology 34:905–908.

Mercalli G, Silvestri O (1891) Le eruzioni dell'isola di Vulcano, incominciate il 3 Agosto 1888 e terminate il 22 Marzo 1890. Relazione Scientifica. Annali dell'Ufficio Centrale di Meteorologia e Geodinamica 10, 4:1–213.

Milano G, Ferrucci F, Guerra I (1989) Interpretazione preliminare di profili DSS del Tirreno meridionale. Proceedings of the National Congress of Gruppo Nazionale di Geofisica della Terra Solida-CNR, Rome, 525–533.

Mollard E, Martel C, Bourdier J.-L (2012) Decompression-induced crystallization in hydrated silica-rich melts: empirical models of experimental plagioclase nucleation and growth kinetics. J Petrol 53:1743–1766.

Morgan D, Jerram DA (2006) On estimating crystal shape for crystal size distribution analysis. J Volcanol Geoth Res 154(1-2):1-7.

Morgavi D, Arzilli F, Pritchard C, Perugini D, Mancini L, Larson P, Dingwell DB (2016). The Grizzly Lake complex (Yellowstone Volcano, USA): Mixing between basalt and rhyolite unraveled by microanalysis and X-ray microtomography. Lithos 260:457–474.

Morimoto N, Fabries J, Ferguson AK, Ginzburg IV, Ross M, Seifert FA, Zussman J, Aoki K, Gottardi D (1988) Nomenclature of pyroxenes. Am Mineral 73, 9-10:1123–1133.

Murphy MD, Sparks RSJ, Barclay J, Carroll MR, Lejeune AM, Brewer TS, Macdonald R, Black S, Young S (1998) The role of magma mixing in triggering the current eruption at the Soufrie're Hills volcano, Montserrat, West Indies. Geophys Res Lett 25:3433–3436.

Nekvasil H, Burnham CW (1987) The calculated individual effects of pressure and water content on phase equilibria in the granite system. In: Mysen BO (ed) Magmatic Processes: Physicochemical Principles. Geo Soc S P 1:433–445.

Nicotra E, Giuffrida M, Viccaro M, Donato P, D'Oriano C, Paonita A, De Rosa R (2018) Timescales of pre-eruptive magmatic processes at Vulcano (Aeolian Islands, Italy) during the last 1000 years. Lithos 316–317, 347–365.

Nimis P (1995) A clinopyroxene geobarometer for basaltic systems based on crystal structure modeling. Contrib Mineral Petrol 121:115–125.

Nimis P, Taylor WR (2000) Single clinopyroxene thermobarometry for garnet peridotites. Part I. Calibration and testing of a Cr-in-Cpx barometer and an enstatite-in-Cpx thermometer. Contrib Mineral Petrol 139:541–544.

Paonita A, Favara R, Nuccio PM, Sortino F (2002) Genesis of fumarolic emissions as inferred by isotope mass balances: CO_2 and water at Vulcano Island, Italy. Geochim Cosmochim Acta 66, 759–772.

Paonita A, Federico C, Bonfanti P, Capasso G, Inguaggiato S, Italiano F, Madonia P, Pecoraino G, Sortino F (2013) The episodic and abrupt geochemical changes at La Fossa fumaroles (Vulcano Island, Italy) and related constraints on the dynamics, structure, and compositions of the magmatic system. Geochim Cosmochim Acta 120, 158–178.

Peccerillo A, Frezzotti ML, De Astis G, Ventura G (2006) Modeling the magma plumbing system of Vulcano (Aeolian Islands, Italy) by integrated fluid-inclusion geobarometry, petrology, and geophysics. Geology 34, 1:17–20.

Peccerillo A, Taylor SR (1976) Geochemistry of Eocene calc-alkaline volcanic rocks of the Kastamonu area northern Turkey. Contrib Mineral Petrol 58:63–81.

Pearce JA (1982) Trace element characteristics of lavas from destructive plate boundaries. From: Thorpe RS (ed) Andesites: Orogenic andesites and related rocks. Wiley, Chichester, pp. 526–547

Perugini D, De Campos CP, Petrelli M, Dingwell DB (2015) Concentration variance decay during magma mixing: A volcanic chronometer. Sci Rep 5, 14225.

Perugini D, Poli G (2005) Viscous fingering during replenishment of felsic magma chambers by continuous inputs of mafic magmas: field evidence and fluid-mechanics experiments. Geology 33:5-8.

Perugini D, Poli G (2011) Frontiers: intrusion of mafic magmas into felsic magma chambers: new insights from natural outcrops and fluid-mechanics experiments. Ital J Geosci 130:3-15.

Perugini D, Poli G (2012) The mixing of magmas in plutonic and volcanic environments: Analogies and differences. Lithos 153:261–277.

Perugini D, Valentini L, Poli G (2007) Insights into magma chamber processes from the analysis of size distribution of enclaves in lava flows: A case study from Vulcano Island (Southern Italy). J Volcanol Geoth Res 166:193–203.

Petrelli M, El Omari K, Spina L, Le Guer Y, La Spina G, Perugini D (2018) Timescales of water accumulation in magmas and implications for short warning times of explosive eruptions. Nat Comms doi:10.1038/s41467-018-02987-6.

Piochi M, De Astis G, Petrelli M, Ventura G, Sulpizio R, Zanetti A (2009) Constraining the recent plumbing system of Vulcano (Aeolian Arc, Italy) by textural, petrological, and fractal analysis: The 1739 A.D. Pietre Cotte lava flow. Geochem Geophys Geosyst 10, No Q01009.

Preece K, Gertisser R, Barclay J, Charbonnie, SJ, Komorowski J-C, Herd RA (2016) Transitions between explosive and effusive phases during the cataclysmic 2010 eruption of Merapi volcano, Java, Indonesia. Bull Volcanol 78:54.

Putirka KD (2005) Igneous thermometers and barometers based on plagioclase + liquid equilibria: tests of some existing models and new calibrations. Am Mineral 90:336–346.

Putirka KD (2008) Thermometers and barometers for volcanic systems. Rev Mineral Geochem 69:61–120.

Putirka KD, Mikaelian H, Ryerson F, Shaw H (2003) New clinopyroxene-liquid thermobarometers for mafic, evolved, and volatile-bearing lava compositions, with applications to lavas from Tibet and the Sanke River Plain, Idaho. Am Mineral 88:1542–1554.

Rossi S, Petrelli M, Morgavi D, González-García D, Fischer LA, Vetere F, Perugini D (2017) Exponential decay of concentration variance during magma mixing: Robustness of a volcanic chronometer and implications for the homogenization of chemical heterogeneities in magmatic systems, Lithos 286-287, 396-407.

Ruch J, Vezzoli L, De Rosa R, Di Lorenzo R, Acocella V (2016) Magmatic control along a strike-slip volcanic arc: the central Aeolian arc (Italy). Tectonics 35, 407–424.

Rudnick, R.L., 1992. Restites, Eu anomalies and the lower continental crust. Geochimica et Cosmochimica Acta 56, 963-970.

Ruprecht, P, Plank T (2013) Feeding andesitic eruptions with a high-speed connection from the mantle. Nature 500, 68–72.

Schneider CA, Rasband WS, Eliceiri KW (2012) NIH Image to ImageJ: 25 years of image analysis. Nature Methods 9:671–675.

Schwarz S, Klügel A, Wohlgemuth-Ueberwasser C (2004) Melt extraction pathways and stagnation depths beneath the Madeira and Desertas rift zones (NE Atlantic) inferred from barometric studies. Contrib Mineral Petrol 147:228–240.

Shane P, Nairn IA, Smith VC (2005) Magma mingling in the similar to 50 ka Rotoiti eruption from Okataina Volcanic Centre: implications for geochemical diversity and chronology of large volume rhyolites. J Volcanol Geoth Res 139, 3–4:295–313.

Shane P, Nairn IA, Smith VC, Darragh M, Beggs K, Cole JW (2008) Silicic recharge of multiple rhyolite magmas by basaltic intrusion during the 22.6 ka Okareka Eruption Episode, New Zealand. Lithos 103:527-549.

Sparks R, Sigurdsson H, Wilson L (1977) Magma mixing: a mechanism for triggering acid explosive eruptions. Nature 267:315–318.

Spell TL, Kyle PR, Thirlwall MF, Campbell AR (1993) Isotopic and geochemical constraints on the origin and evolution of postcollapse rhyolites in the Valles Caldera, New Mexico. J Geophys Res 98:723-739.

Stroncik NA, Klügel A, Hansteen TH (2009) The magmatic plumbing system beneath El Hierro (Canary Islands): constraints from phenocrysts and naturally quenched basaltic glasses in submarine rocks. Contrib Mineral Petrol 157:593–607.

Taylor SR, McLennan SM (1985) The continental crust: its composition and evolution. Blackwell Scientific Publication, Carlton, 312 p

Ventura G, Vilardo G, Milano G, Pino NA (1999) Relationships among crustal structure, volcanism and strike-slip tectonics in the Lipari-Vulcano volcanic complex (Aeolian Islands, Southern Tyrrhenian Sea, Italy). Phys Earth Planet Inter 116:31–52.

Vetere F, Petrelli M, Morgavi D, Perugini D (2015) Dynamics and time evolution of a shallow plumbing system: The 1739 and 1888–90 eruptions, Vulcano Island, Italy. J Volcanol Geoth Res 306:74–82.

Waight TE, Dean AA, Mass R, Nicholls IA (2000) Sr and Nd isotopic investigations towards the origin of feldspar megacrysts in microgranular enclaves in two I-type plutons of the Lachlan Fold Belt, southeast Australia. Austr Jour Earth Sci 47:1105-1112.

Wang CY, Hwang WT, Shi Y (1989) Thermal evolution of a rift basin: The Tyrrhenian Sea. J Geophys Res 94:3991–4006.

Wen S, Nekvasil H (1994) SOLVCALC; an interactive graphics program package for calculating the ternary feldspar solvus and for two-feldspar geothermometry. Comput Geosci 20, 6:1025–1040.

Wolff JA, Ellis BS, Ramos FC, Starkel WA, Boroughs S, Olin PH, Bachmann O (2015) Remelting of cumulates as a process for producing chemical zoning in silicic tuffs: a comparison of cool, wet and hot, dry rhyolitic magma systems. Lithos 236–237:275–286.

Wörner G, Schmincke HU (1984) Mineralogical and chemical zonation of the Laacher See tephra sequence. J Petrol 25:805-835.

Zanon V, Frezzotti M, Peccerillo A (2003) Magmatic feeding system and crustal magma accumulation beneath Vulcano Island (Italy): Evidence from CO_2 fluid inclusions in quartz xenoliths. J Geophys Res 108(B6):2298.

Zingg T (1935) Beitrag zur Schotteranalyse. Schweiz Mineral Petrogr Mitt 15:39-140.

Figures

Fig. 1. (a) Map of the Aeolian archipelago, South Tyrrhenian Sea (Italy), with Vulcano in the centre. Also shown is the Tindari-Letojanni fault system through Lipari and Vulcano (Ventura, 2013). (b) Sketch map of northern Vulcano, showing the Pietre Cotte lava flow on the northern slope of the Fossa Cone. (c) Google Earth image of Pietre Cotte lava flow and (inset) front of flow exhibiting rhyolite host (light) and enclaves (dark). (d) Geological sketch map of Vulcano eruptive epochs and their corresponding synthems (after Keller, 1980; De Astis et al., 2013).

Fig. 2. Photographs of enclaves in host rhyolite, Pietre Cotte lava flow. (a) Rounded with crenulated and lobate contact with host, and (b) shows more angular enclaves.

Fig. 3. Scanning electron microscopy (SEM) images of Pietre Cotte obsidian, enclaves, and mineral assemblages. (a) Olivine and magnetite glomerocryst separated into rhyolitic host, with spherulites nucleating at edge. (b) Fine microlitic enclave groundmass. (c) Glomerocryst of plagioclase, clinopyroxene and magnetite within enclave.

Fig. 4. Interface between enclaves and the rhyolitic host. (a) Cuspate, rounded edge of enclave. (b-f) examples of variable textural coarseness of enclave groundmass near the outer edge of the enclave, interstitial glass, crenulated edges of the enclave, and surrounding vesiculation in the rhyolitic host.

Fig. 5. Examples of disequilibrium textures in macrocrysts (crystals >500 μm) within enclaves. (a) Compositionally zoned plagioclase, with increasing K content towards the edge. (b) Plagioclase surrounded by slightly coarser enclave groundmass. (c) prismatic, unzoned plagioclase in fine grained groundmass. (d-e) plagioclase core with outer alkali feldspar rim. (f) Resorbed plagioclase with magnetite inclusions at the edge. (g-h) compositionally zoned clinopyroxene minerals.

Fig. 6. Plots of morphological properties of measured enclaves. (a) cross-plot of length vs. width of identified rounded enclaves and angular enclaves, (b) shape morphology classification scheme adapted from Zingg, (1935), showing the majority of enclaves are (on average) equant (spherical) in shape, (c) rose diagrams of preferred orientation of enclave long axes, (d) best-fit ellipsoids (rose of boundary sections giving a characteristic shape) of enclaves based on long axes orientations, and (e) representative 3D shape (overall dimensions, excluding crenulations).

Fig. 7. (a) Total alkalis vs SiO_2 diagram (Le Bas et al., 1986) for Pietre Cotte and other Fossa Cone and Vulcano rocks post-50 ka, possibly related to the Fossa Caldera early phases (e.g. Gioncada et al., 2003). Analyses from this study include whole rock ICP-MS of enclave materials, EMPA of interstitial groundmass glass within enclaves, and EMPA (of the obsidian glass host) and ICP-MS (whole rock) of the rhyolitic host. Additional basaltic to trachytic data from De Astis et al. (1997; 2013), Del Moro et al. (1998), Gioncada et al. (1998), Piochi et al. (2009) and Nicotra et al. (2018); grey diamonds with black outline represent Pietre Cotte enclave data from the literature sources, grey diamonds with no outline represent other Fossa Cone products. Teph. Bas. = Tephrite basanite; Basaltic-tr-and. = Basaltic trachyandesite; Trachy-and. = Trachyandesite. (b) K_2O v. SiO_2 classification diagram (Peccerillo and Taylor, 1976) for Pietre Cotte rocks and other Fossa Cone products (see key and literature sources in Fig. 7a). Shosh = Shoshonitic; Bas. And. = Basaltic andesite; CA Series = Calc-Alkaline Series; HKCA Series = High-K Calc-Alkaline Series.

Fig. 8. (a) Chondrite-normalised REE diagram and (b) N-MORB-normalised trace element spider diagram of trachytic enclave material and rhyolitic host. Normalising values from Sun and McDonough (1989). Additional Fossa data from De Astis et al. (1997; 2013), Del Moro et al. (1998) and Gioncada et al. (1998), and Pietre Cotte enclave data from Piochi et al. (2009).

Fig. 9. Major element variation diagrams vs SiO_2 (wt %) for the Pietre Cotte enclaves (whole rock and interstitial groundmass glass) and rhyolitic host. All analyses are normalised to 100 wt%, free of volatiles. Additional Pietre Cotte enclave data from De Astis et al. (1997; 2013), Del Moro et al. (1998), Gioncada et al. (1998), Piochi et al. (2009) and Nicotra et al. (2018).

Fig. 10. Variation diagrams for Rb, V, Ba, Zr, Sr and Nb (determined by ICP-MS vs. SiO_2). Additional Pietre Cotte enclave data from De Astis et al. (1997; 2013), Del Moro et al. (1998), Gioncada et al. (1998), Piochi et al. (2009) and Nicotra et al. (2018).

Fig. 11. Modelled evolution of the Pietre Cotte rhyolitic host through assimilation and fractional crystallisation (AFC) processes, with fractional crystallisation (FC) curve also calculated. AFC and FC curves computed from shoshonitic crystal mush composition and a heterogeneous assimilated

Calabro-Peloritano basement crust of Frezzotti et al. (2004). *r* = Assimilation rate/fractionation rate. r value set at 0.2 and 0.5 in order to mimic fractionation-dominant and assimilation-dominant regimes (Albarede, 1995; De Astis et al., 1997).

Fig. 12. Pietre Cotte enclave and rhyolitic host mineral chemistry. (a) Feldspar ternary classification diagrams for Pietre Cotte enclave plagioclase and alkali feldspar phenocrysts and groundmass crystals. (b) Pyroxene ternary classification diagram (Morimoto et al., 1988) for Pietre Cotte enclave clinopyroxene (yellow circles), and superimposed olivine classification (green boxes and text). (c) Ternary classification of analysed oxide minerals in Pietre Cotte enclaves and obsidian host.

Fig. 13. Clinopyroxene equilibrium test, comparing observed and predicted values for clinopyroxene components ($K_D(Fe\text{-}Mg)_{cpx\text{-}liq}$; Putirka, 2008). Published data (blue triangles) includes latitic-trachytic compositions from De Astis et al. (1997; 2013), Del Moro et al. (1998), Gioncada et al. (1998) and Piochi et al. (2009). Bold 1:1 line represents a fully equilibrated system, and progressive departure of data points from line indicates decreasing degree of equilibrium.

Fig. 14. SOLVCALC orthoclase-plagioclase trachytic groundmass equilibria and temperature/pressure estimations (Wen and Nekvasil, 1994).

Fig. 15. Model of magmatic processes occurring in the Fossa Cone magmatic system, leading to the Pietre Cotte lava flow.

Tables

Table 1. Average enclave shape/size parameters for all enclaves and identified enclave types (more rounded and more angular enclaves) from field samples, calculated using ImageJ software. Mean diameter parameter represents longest distance between any two points along the selection boundary; Circularity ranges from 0 (infinitely elongated polygon) to 1 (perfect circle) (Ferreira and Rasband, 2012).

Table 2. ICP-AES major element (wt%) compositions of Pietre Cotte whole rock enclave and obsidian host products.

Table 3. ICP-MS trace element (ppm) compositions of Pietre Cotte whole rock enclave products.

Table 4. ICP-MS trace element (ppm) compositions of Pietre Cotte obsidian host volcanics.

Table 5. EMPA glass compositional spot analyses (wt%) of Pietre Cotte enclave interstitial groundmass glass.

Table 6. EMPA glass compositional spot analyses (wt%) of Pietre Cotte obsidian host.

Table 7. Intensive variable calculations of pressure and temperature associated with each magma of the Pietre Cotte magmatic system.

Table 1. Average enclave shape/size parameters for all enclaves and identified enclave types (more rounded and more rigid enclaves) from field samples, calculated using *ImageJ* software. Mean diameter parameter represents longest distance between any two points along the selection boundary; Circularity ranges from 0 (infinitely elongated polygon) to 1 (perfect circle) (Ferreira and Rasband, 2012).

	Number of analysed enclaves	Area of host lava occupied (%)	Mean perimeter (mm)	Perimeter range (mm)	Circularity index	Solidity index	Mean diameter (mm)	Diameter range (mm)
All analysed enclaves	968	4.4	87.1	4.7-190.3	0.89	0.90	33.5	1.8-70.6
Rounded enclaves	771	6.3	86.0	4.7-120.7	0.92	0.89	33.1	1.8-38.2
Rigid enclaves	199	1.1	107.5	5.0-190.3	0.82	0.90	41.4	5.0-70.6

Table 2. ICP-AES major element (wt%) compositions of Pietre Cotte whole rock enclave and obsidian host products.

	Whole rock enclave (wt%)														Whole roc	
	PCEN C1	PCEN C2	PCEN C3	PCEN C4	PCEN C5	PCEN C6	PCEN C7	PCEN C8	PCEN C9	PCEN C10	PCEN C10-2	PCEN C11	PCEN C12	PCEN C13	PCOB S1	PC S2
Major elements (ICP-MS)																
SiO_2	52.70	53.30	52.30	52.80	52.80	52.00	51.70	52.20	52.30	52.30	51.60	51.50	52.90	51.30	72.90	73
TiO_2	0.76	0.78	0.77	0.77	0.78	0.77	0.78	0.78	0.78	0.77	0.75	0.78	0.78	0.79	<0.01	<0
Al_2O_3	17.55	17.55	17.40	17.40	17.45	17.15	17.15	17.30	17.70	17.15	17.10	17.10	17.95	17.20	13.20	13
Fe_2O_3	10.35	10.50	10.10	10.10	10.25	10.10	10.20	10.25	10.45	10.10	9.95	10.20	10.45	10.35	2.19	2
MnO	0.17	0.17	0.18	0.18	0.18	0.18	0.17	0.18	0.17	0.18	0.17	0.18	0.17	0.18	0.11	0
MgO	4.01	4.14	4.02	4.06	4.07	4.00	4.03	4.05	4.02	4.05	3.98	4.05	4.17	4.08	0.23	0
CaO	8.73	8.84	8.92	8.97	9.01	8.86	8.84	8.92	8.80	8.87	8.70	8.83	8.95	8.84	1.10	1
Na_2O	3.07	3.06	2.99	3.00	3.00	2.96	2.94	2.96	3.10	2.97	2.98	2.94	2.92	2.95	4.17	4
K_2O	1.34	1.31	1.39	1.42	1.40	1.41	1.37	1.38	1.35	1.33	1.32	1.39	1.36	1.31	4.89	4
P_2O_5	0.19	0.18	0.20	0.19	0.21	0.19	0.19	0.20	0.19	0.20	0.20	0.19	0.20	0.19	0.08	0
SrO	0.09	0.09	0.09	0.08	0.08	0.08	0.08	0.08	0.08	0.08	0.08	0.08	0.06	0.09	0.03	0
BaO	0.04	0.04	0.04	0.04	0.04	0.04	0.04	0.04	0.04	0.04	0.04	0.04	0.04	0.04	0.01	0
LOI	1.35	1.33	1.37	1.37	1.42	1.35	1.37	1.38	1.37	1.42	1.42	1.36	1.36	1.38	0.59	0
Total	100.35	101.29	99.77	100.38	100.69	99.09	98.86	99.72	100.35	99.46	98.29	98.64	101.31	98.70	99.50	99

Table 3. ICP-MS trace element (ppm) compositions of Pietre Cotte whole rock enclave products.

	Whole rock enclave (ppm)									
	PCENC1	PCENC2	PCENC3	PCENC4	PCENC5	PCENC6	PCENC7	PCENC8	PCENC9	PCENC10
Trace elements (ICP-MS)										
Ba	360	375	379	376	353	372	370	376	384	384
Ce	36.3	37.7	37.4	37.3	35.9	37.4	36.2	38	38.5	37.8
Cr	<10	<10	<10	<10	<10	<10	<10	<10	<10	<10
Cs	0.58	0.59	0.58	0.57	0.57	0.64	0.65	0.64	0.68	0.7
Dy	3.17	3.54	3.36	3.39	3.4	3.22	3.22	3.25	3.3	3.29
Er	2	2.1	2.02	2.11	1.94	1.97	1.98	2.02	1.96	2.08
Eu	1.17	1.22	1.09	1.11	1.12	1.08	1.11	1.12	1.15	1.19
Ga	17.2	18	17.2	18.3	17.2	18	18.1	18.9	18	18.7
Gd	3.23	3.28	3.38	3.44	3.21	3.27	3.31	3.45	3.41	3.36
Hf	1.8	1.7	1.8	1.8	1.7	1.7	1.8	1.9	1.9	1.8
Ho	0.69	0.72	0.71	0.67	0.69	0.65	0.68	0.72	0.72	0.68
La	16.9	16.9	17.4	17.6	16.6	17.2	17.5	17.6	17.7	18
Lu	0.32	0.31	0.32	0.31	0.31	0.31	0.3	0.31	0.32	0.32
Nb	4.5	4.3	4.1	3.9	3.8	3.7	3.4	4	3.6	3.6
Nd	17	17.1	17.8	17.2	16.5	17	16.8	17.1	17.6	17.5
Pr	4.07	4.2	4.21	4.37	4	4.11	4.12	4.16	4.3	4.2
Rb	31	31.8	31.2	32.1	29.8	31.6	32	31.9	33.3	33.2
Sm	3.89	3.81	4.14	3.99	3.73	3.75	3.87	4.07	3.98	3.88
Sn	1	1	1	1	1	1	1	1	1	1
Sr	706	709	697	736	676	699	716	676	703	703
Ta	0.7	0.6	0.7	0.6	0.6	0.6	0.6	0.7	0.5	0.4
Tb	0.52	0.56	0.55	0.53	0.52	0.54	0.53	0.57	0.52	0.54
Th	3.53	3.65	3.57	3.56	3.46	3.41	3.44	3.43	3.62	3.84
Tm	0.31	0.31	0.3	0.29	0.31	0.3	0.3	0.28	0.32	0.3
U	1.22	1.27	1.24	1.32	1.26	1.28	1.27	1.2	1.26	1.4
V	297	295	306	317	294	299	295	301	299	301
W	198	197	194	196	190	199	193	188	132	75
Y	18.1	17.8	18.3	18.3	17.4	18	18.1	17.8	18.2	18.2
Yb	2.06	2.21	2.15	2	2.11	2.04	2.04	2.09	2.28	2.08
Zr	66	65	63	64	62	65	63	65	65	64

Table 4. ICP-MS trace element (ppm) compositions of Pietre Cotte obsidian host volcanics.

	Whole rock obsidian host (ppm)						
	PCOBS1	PCOBS2	PCOBS3	PCOBS4	PCOBS5	PCOBS6	PCOBS7
Trace elements (ICP-MS)							
Ba	76.4	71.9	70.5	73.2	72.4	68.2	70.7
Ce	136.5	133	130.5	134.5	136.5	131	132.5
Cr	10	<10	<10	<10	<10	<10	<10
Cs	16.65	16.1	15.95	16	16.35	15.8	16
Dy	6.66	6.19	6.55	6.62	6.84	6.52	6.83
Er	4.19	4.23	4.35	3.99	4.33	4.03	4.22
Eu	0.26	0.25	0.25	0.25	0.26	0.26	0.27
Ga	19.5	18.5	18.8	18.6	18.9	18.4	18.1
Gd	6.52	6.44	6.61	6.28	6.57	6.5	6.41
Hf	7.2	7.1	7.5	7.3	7.5	7.1	7.5
Ho	1.3	1.34	1.38	1.38	1.39	1.33	1.33
La	74	72.1	69.9	71.2	72.2	70.3	71.3
Lu	0.7	0.73	0.7	0.68	0.7	0.71	0.69
Nb	37.9	36.1	35.8	35.1	36.8	35.3	35.2
Nd	46.2	45.2	44.8	46.2	45.9	44.3	45.6
Pr	13.5	13.25	13.15	13.4	13.6	12.9	13.25
Rb	298	293	285	286	292	282	284
Sm	9.27	8.96	8.31	8.8	9.35	8.7	8.68
Sn	8	8	8	8	8	8	8
Sr	76.9	73.8	71.8	70.9	74.7	70.7	70.2
Ta	3.4	3.2	3.2	3.3	3.3	3.3	3.4
Tb	1.08	1.13	1.09	1.08	1.11	1.05	1.13
Th	58.9	59.5	59	58.5	59.6	58.5	60.6
Tm	0.69	0.65	0.68	0.7	0.68	0.69	0.69
U	17	17.05	17.45	17	17.7	16.85	17.65
V	10	8	6	7	11	7	8
W	319	313	313	314	311	306	309
Y	39.3	38.6	37.9	38	39.4	36.5	37
Yb	4.61	4.88	4.76	4.75	4.7	4.66	4.82
Zr	224	218	218	214	227	208	209

Table 5. EMPA glass compositional spot analyses (wt%) of Pietre Cotte enclave glassy inclusions.

	Glass analyses enclave (wt%)									
Sample:	TR1-M38	TR22	TR23	TR21	TR25	TR19	TR18	TR31	TR17	TR26
Major elements (EMPA)										
SiO_2	63.01	63.46	62.77	61.96	61.46	61.91	60.96	61.10	61.00	60.70
TiO_2	0.50	0.10	0.30	0.49	0.39	0.29	0.59	0.65	0.39	0.51
Al_2O_3	19.00	18.25	18.91	17.98	19.27	18.45	21.67	18.49	18.64	19.17
Fe_2O_3	4.26	4.39	4.55	5.60	4.02	3.80	4.18	4.67	6.05	4.47
MnO	0.14	0.10	0.11	0.18	0.05	0.11	0.06	0.06	0.17	0.13
MgO	1.52	0.61	0.80	1.09	0.74	1.15	0.58	1.19	1.07	1.08
CaO	2.41	2.67	1.41	1.90	2.14	2.94	1.89	1.11	1.71	2.35
Na_2O	5.05	5.31	5.13	4.43	5.76	4.98	4.89	4.52	4.94	4.96
K_2O	3.22	4.75	5.70	5.98	4.46	4.93	5.55	6.32	5.14	5.17
P_2O_5	0.00	0.00	0.00	0.00	0.00	0.00	0.00	0.00	0.00	0.00
Total	99.11	99.64	99.68	99.61	98.29	98.56	100.37	98.11	99.11	98.54

Table 6. EMPA glass compositional spot analyses (wt%) of Pietre Cotte obsidian host.

	Glass analyses obsidian host (wt%)																
Sample:	Vulc-1	Vulc-2	Vulc-3	Vulc-4	Vulc-5	Vulc-6	Vulc-7	Vulc-8	Vulc-9	Vulc-10	Vulc-11	Vulc-12	Vulc-2rr	Vulc-3rr	Vulc-4rr	VulcNG-1	VulcNG5rr
Major elements (EMPA)																	
SiO_2	77.11	76.94	76.95	75.60	75.59	76.03	77.03	77.05	76.53	76.60	76.96	76.10	75.95	74.74	75.59	74.70	74.16
TiO_2	0.13	0.05	0.07	0.13	0.11	0.10	0.09	0.07	0.10	0.10	0.11	0.12	0.13	0.12	0.10	0.08	0.12
Al_2O_3	13.51	13.19	13.35	13.63	13.28	13.53	13.65	13.73	13.94	13.52	13.47	13.64	13.29	13.06	12.99	13.26	13.14
Fe_2O_3	1.63	1.55	1.59	1.90	1.76	1.76	1.54	1.78	1.62	1.74	1.66	1.47	1.65	1.78	1.59	1.80	1.73
MnO	0.07	0.06	0.07	0.06	0.06	0.07	0.03	0.06	0.05	0.06	0.07	0.06	0.07	0.07	0.07	0.09	0.07
MgO	0.04	0.03	0.03	0.06	0.05	0.06	0.04	0.05	0.05	0.05	0.05	0.04	0.04	0.06	0.02	0.06	0.06
CaO	0.65	0.61	0.61	0.63	0.63	0.68	0.72	0.66	0.65	0.60	0.66	0.79	0.56	0.59	0.56	0.68	0.59
Na_2O	2.74	2.86	3.08	3.24	2.79	3.20	3.62	3.21	3.28	3.26	3.08	4.10	4.38	4.61	4.21	3.60	4.83
K_2O	3.96	4.00	3.73	3.94	3.68	3.73	3.83	3.93	3.95	3.82	3.83	3.58	4.28	4.68	3.98	4.26	3.77
P_2O_5	0.06	0.01	0.02	0.03	0.02	0.00	0.01	0.03	0.01	0.01	0.01	0.02	0.01	0.03	0.00	0.01	0.04
Total	99.84	99.29	99.47	99.22	97.97	99.18	100.57	100.56	100.10	99.76	99.90	99.91	100.35	99.74	99.11	98.53	98.51

Table 7. Intensive variable calculations of pressure and temperature associated with each magma of the Pietre Cotte magmatic system. See methodology for model parameter inputs.

	Pressure (MPa)	Method of pressure calculation	Maximum depth (km)	Temperature (Deg C)	Method of temperature calculation
Basalt cumulate	825 (±80)	Clinopyroxene-melt barometry of Putirka et al. (2003)	28	789-1117	QUILF thermometry of Andersen et al. (1993)
Shoshonite	707 (±80)	Clinopyroxene-melt barometry of Putirka et al. (2003)	26	1089-1149	Clinopyroxene-melt thermometry of Putirka et al. (2003)
Trachyte	640 (±74)	Clinopyroxene-melt barometry of Putirka et al. (2003)	23	1000-1130	SolvCalc method of Wen and Nekvasil (1994)
Rhyolite	60 (see refs)	Prev. fluid inclusion studies (Clocchiatti et al., 1994; Zanon et al., 2003)	4	953-979	Rhyolite-MELTS liquidus thermometry of Gualda et al. (2012)

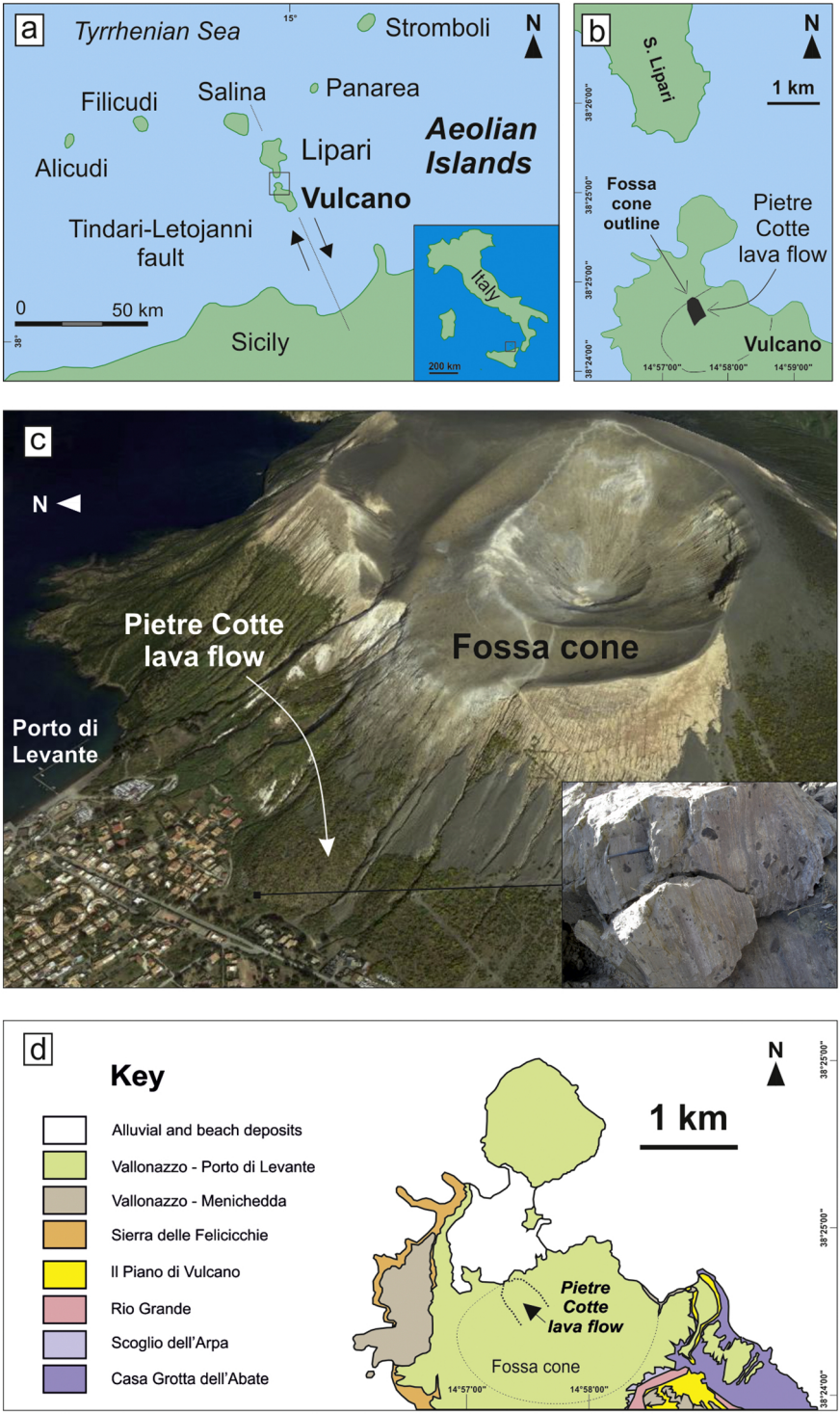
a
Tyrrhenian Sea
Stromboli
N
Filicudi
Salina
Panarea
Aeolian Islands
Alicudi
Lipari
Vulcano
Tindari-Letojanni fault
0
50 km
Sicily
Italy
200 km
b
S. Lipari
N
1 km
Fossa cone outline
Pietre Cotte lava flow
Vulcano
c
N
Pietre Cotte lava flow
Fossa cone
Porto di Levante
d
Key
Alluvial and beach deposits
Vallonazzo - Porto di Levante
Vallonazzo - Menichedda
Sierra delle Felicicchie
Il Piano di Vulcano
Rio Grande
Scoglio dell'Arpa
Casa Grotta dell'Abate
N
1 km
Pietre Cotte lava flow
Fossa cone

Figure 1

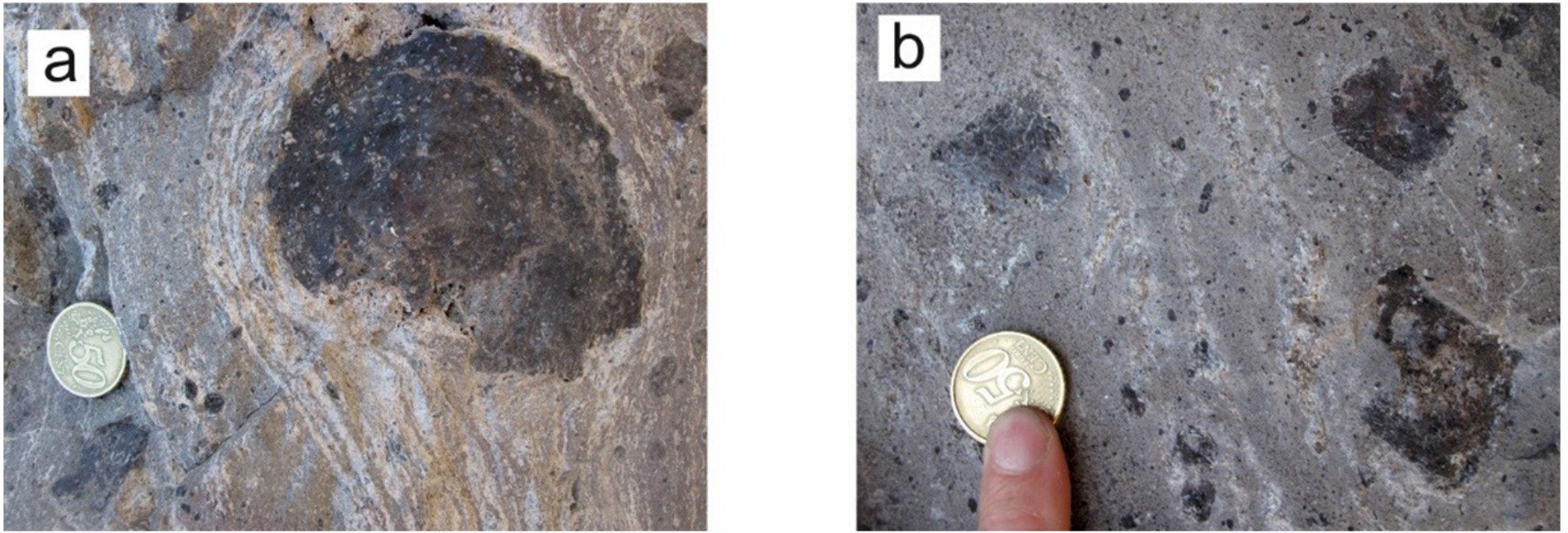

Figure 2

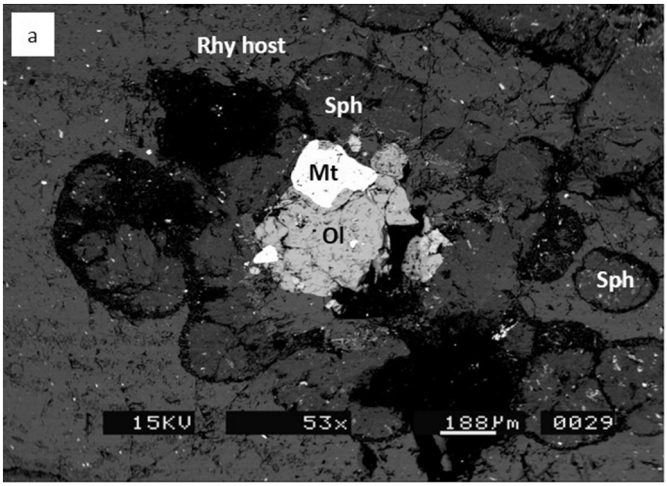
a
Rhy host
Sph
Mt
Ol
Sph
15KV
53x
188µm
0029

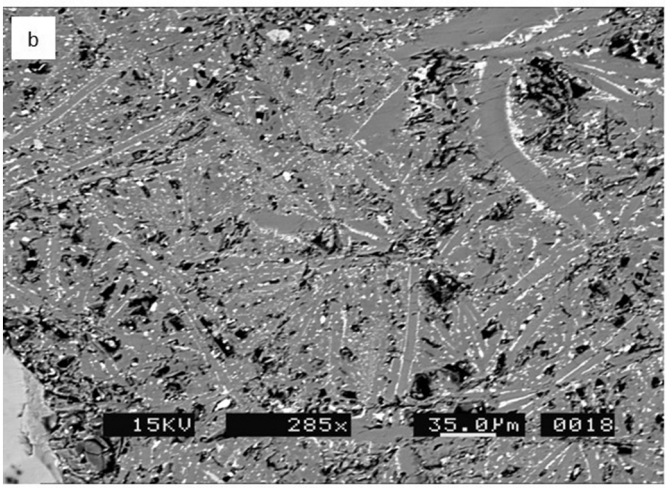
b
15KV
285x
35.0µm
0018

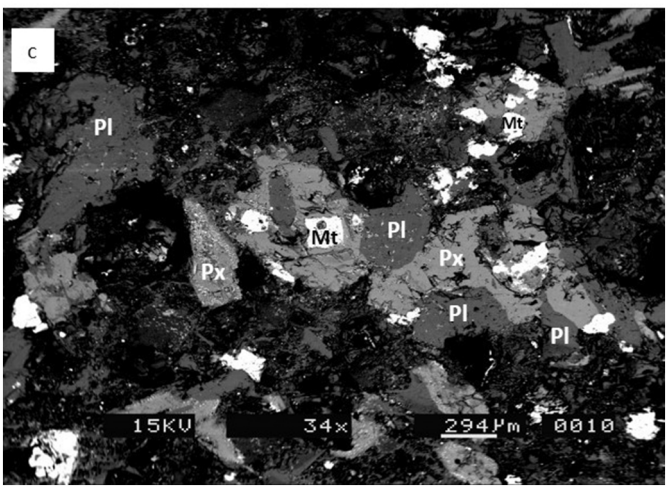
c
Pl
Mt
Mt
Pl
Px
Px
Pl
Pl
15KV
34x
294µm
0010

Figure 3

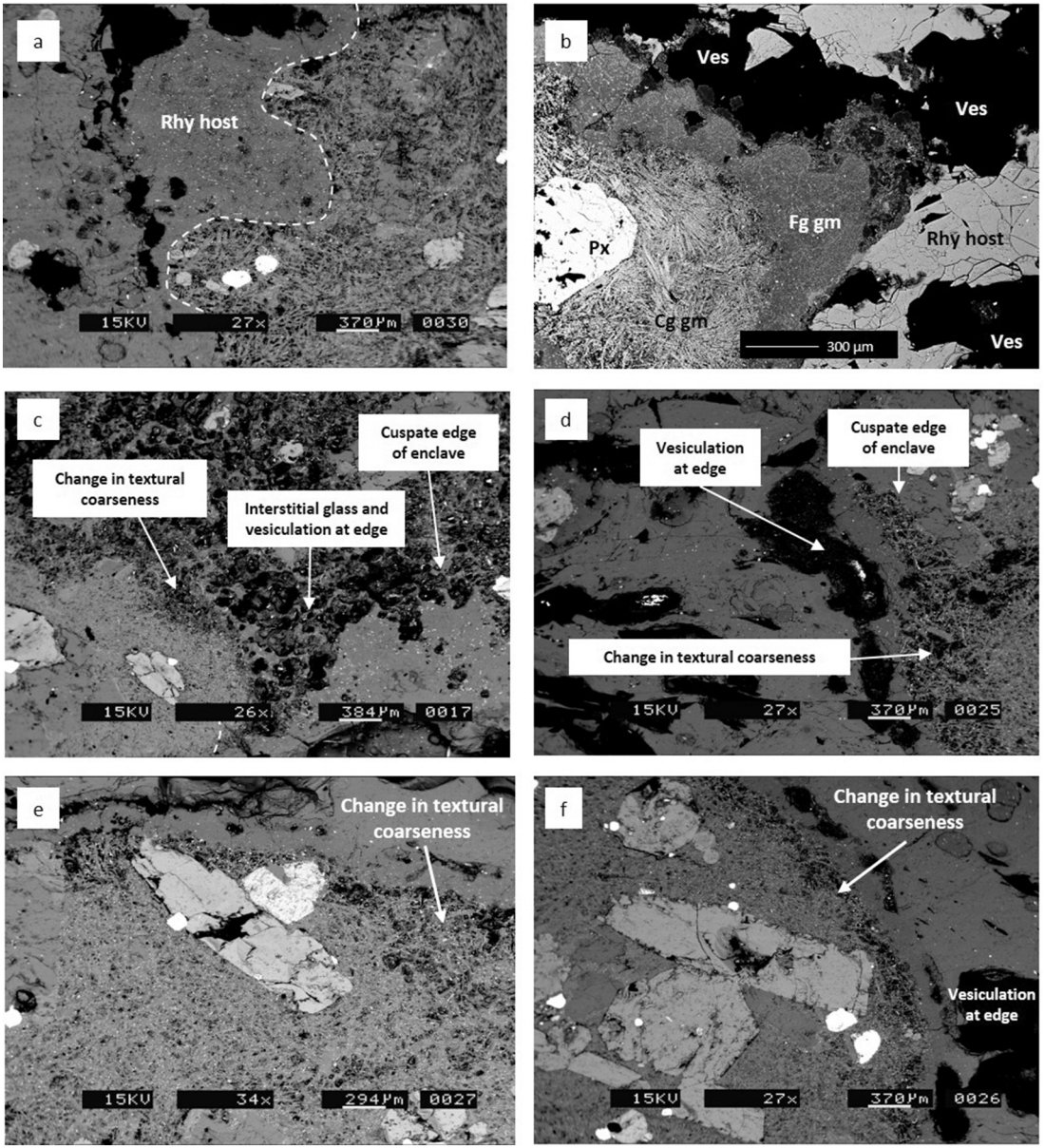
a
Rhy host
15KV 27× 370µm 0030
b
Ves
Ves
Fg gm
Px
Rhy host
Cg gm
300 µm
Ves
c
Cuspate edge of enclave
Change in textural coarseness
Interstitial glass and vesiculation at edge
15KV 26× 384µm 0017
d
Vesiculation at edge
Cuspate edge of enclave
Change in textural coarseness
15KV 27× 370µm 0025
e
Change in textural coarseness
15KV 34× 294µm 0027
f
Change in textural coarseness
Vesiculation at edge
15KV 27× 370µm 0026

Figure 4

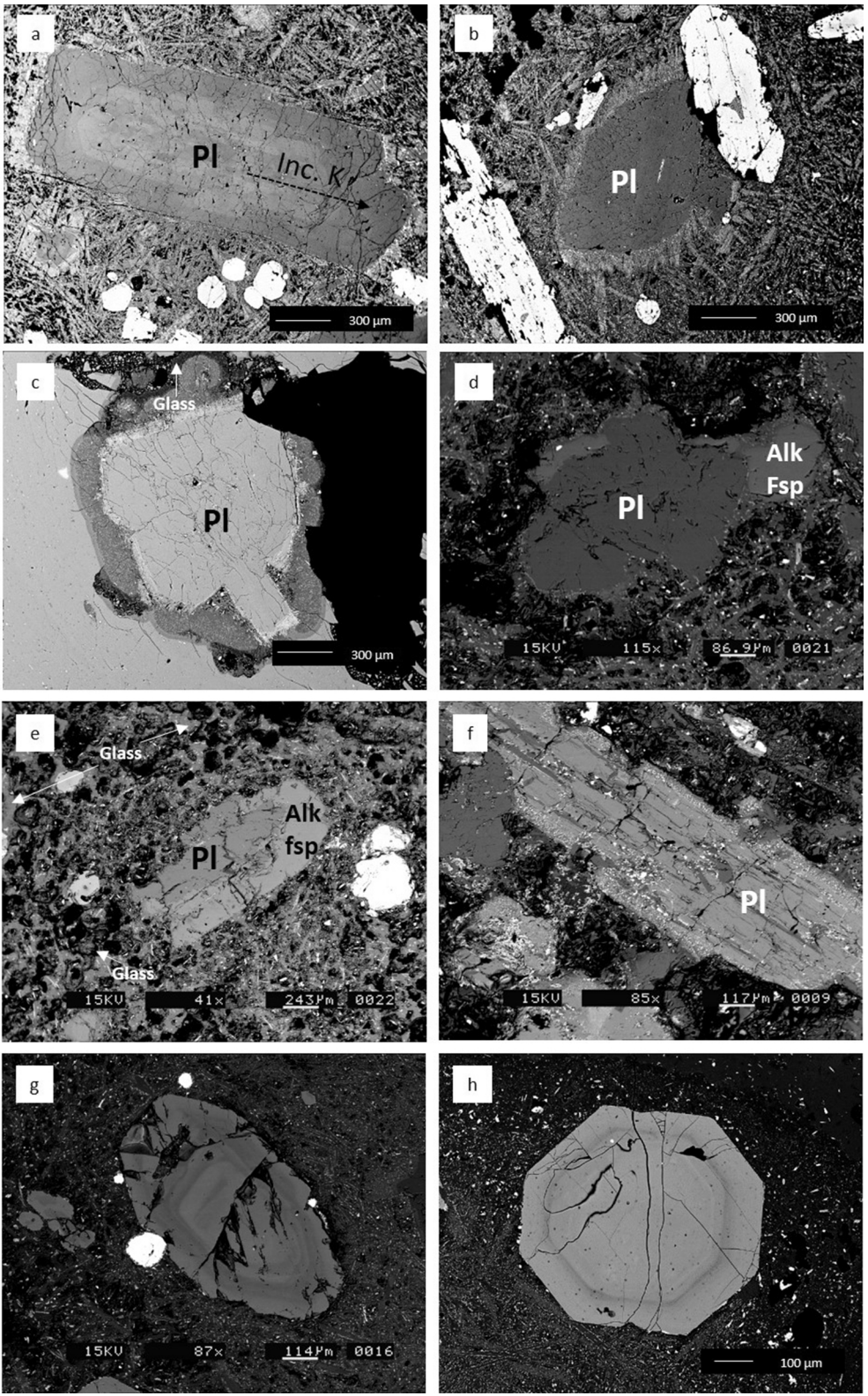
a
Pl
Inc. K
300 µm
b
Pl
300 µm
c
Glass
Pl
300 µm
d
Alk
Fsp
Pl
15KV 115x 86.9µm 0021
e
Glass
Alk
fsp
Pl
Glass
15KV 41x 243µm 0022
f
Pl
15KV 85x 117µm 0009
g
15KV 87x 114µm 0016
h
100 µm

Figure 5

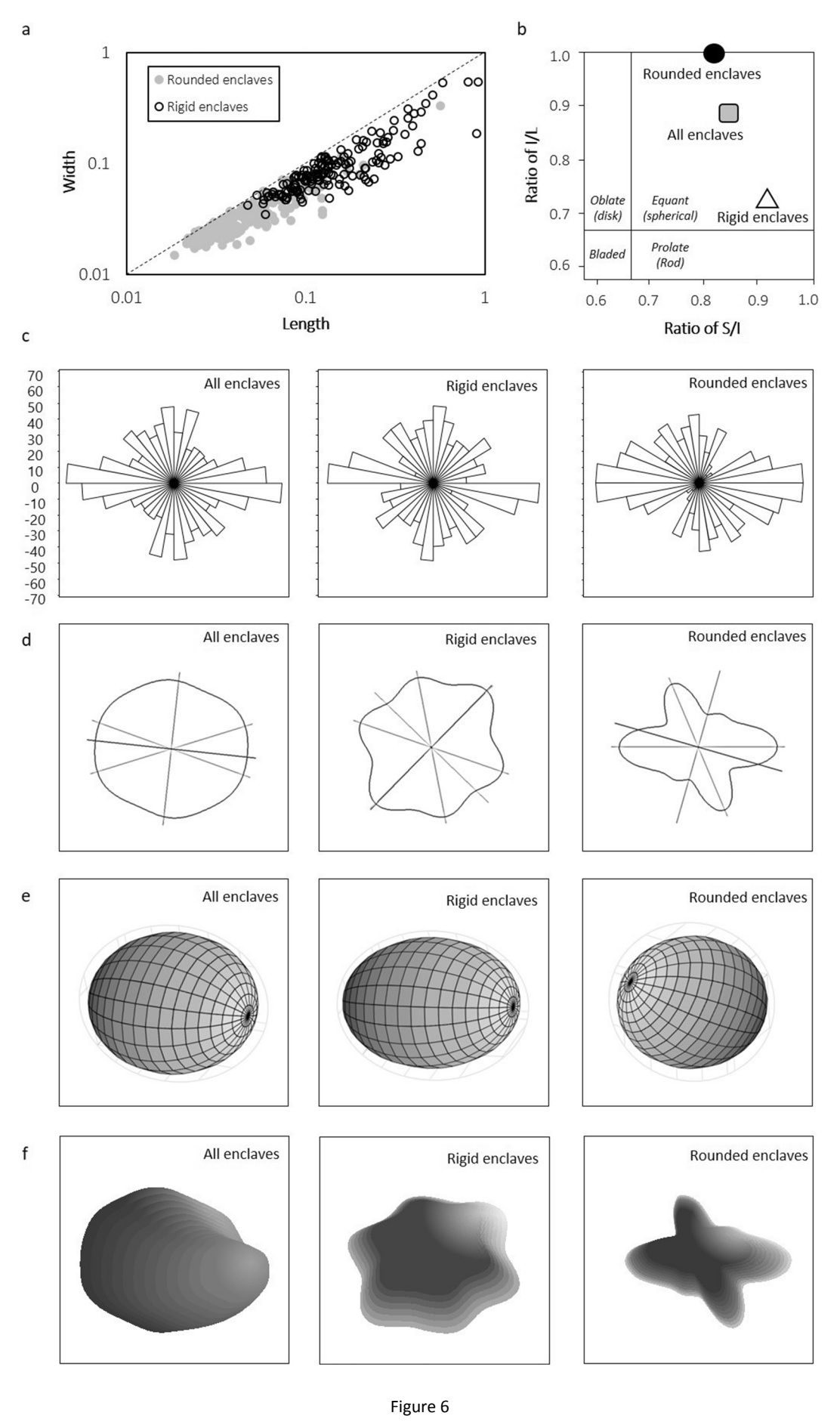
a
Rounded enclaves
Rigid enclaves
Width
Length
1
0.1
0.01
0.01
0.1
1
b
Rounded enclaves
All enclaves
Rigid enclaves
Ratio of I/L
Ratio of S/I
Oblate (disk)
Equant (spherical)
Bladed
Prolate (Rod)
1.0
0.9
0.8
0.7
0.6
c
All enclaves
Rigid enclaves
Rounded enclaves
70
60
50
40
30
20
10
0
-10
-20
-30
-40
-50
-60
-70
d
All enclaves
Rigid enclaves
Rounded enclaves
e
All enclaves
Rigid enclaves
Rounded enclaves
f
All enclaves
Rigid enclaves
Rounded enclaves

Figure 6

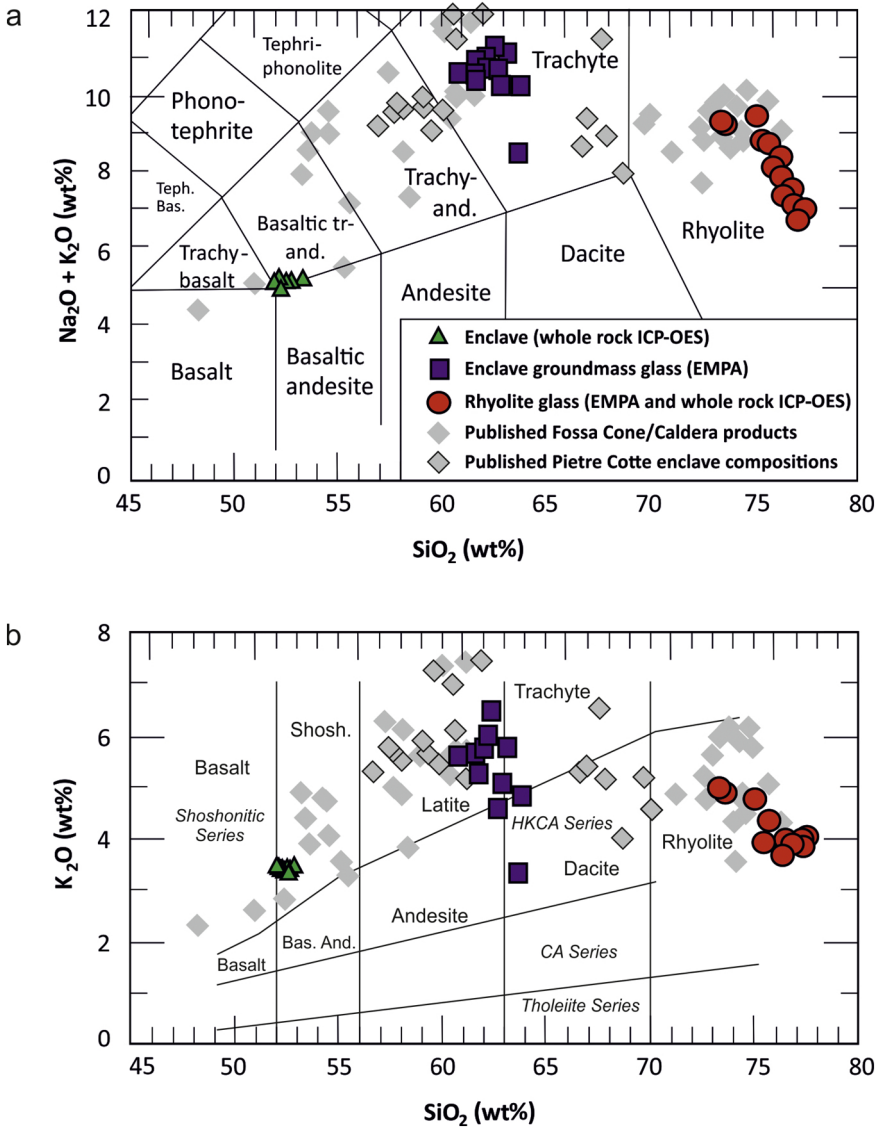
a
Tephri-
phonolite
Trachyte
Phono-
tephrite
Teph.
Bas.
Trachy-
and.
Basaltic tr-
and.
Rhyolite
Trachy-
basalt
Dacite
Andesite
Basalt
Basaltic
andesite
Enclave (whole rock ICP-OES)
Enclave groundmass glass (EMPA)
Rhyolite glass (EMPA and whole rock ICP-OES)
Published Fossa Cone/Caldera products
Published Pietre Cotte enclave compositions
Na2O + K2O (wt%)
SiO2 (wt%)
b
Trachyte
Shosh.
Basalt
Latite
Shoshonitic
Series
HKCA Series
Rhyolite
Dacite
Andesite
Bas. And.
Basalt
CA Series
Tholeiite Series
K2O (wt%)
SiO2 (wt%)

Figure 7

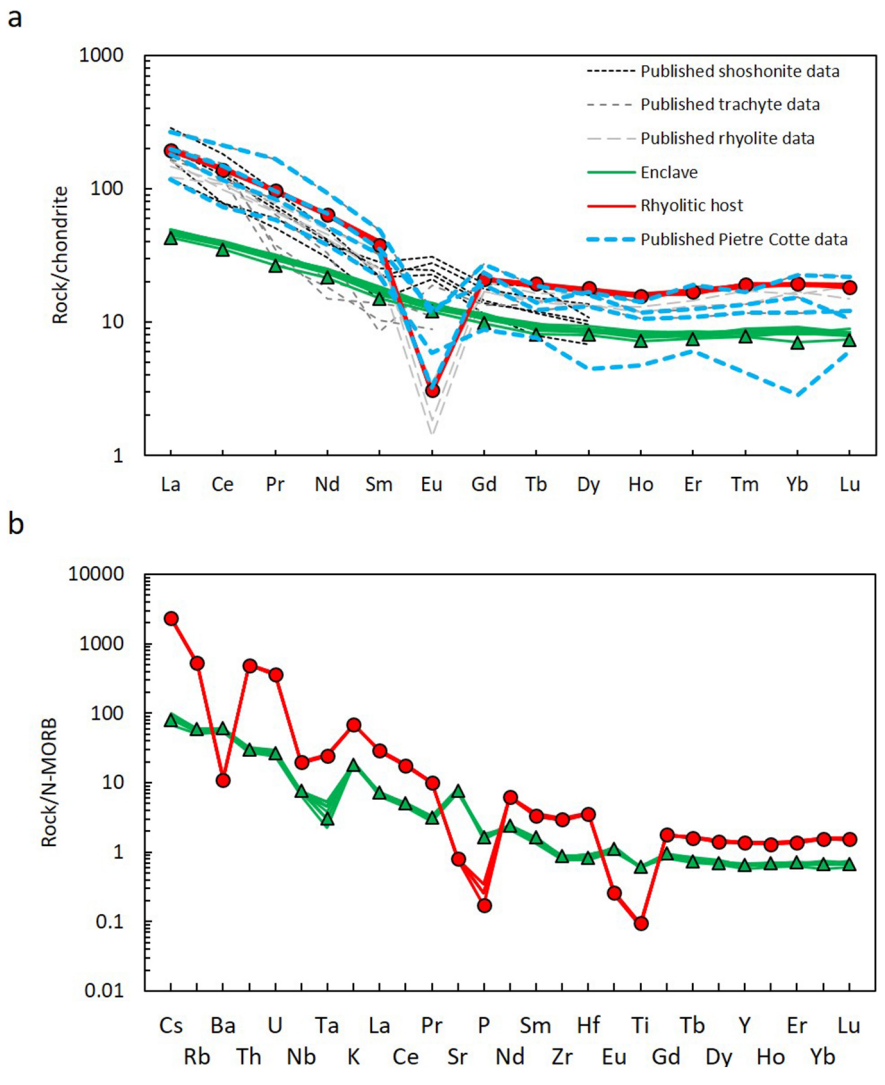
a
1000
100
10
1
Rock/chondrite
Published shoshonite data
Published trachyte data
Published rhyolite data
Enclave
Rhyolitic host
Published Pietre Cotte data
La Ce Pr Nd Sm Eu Gd Tb Dy Ho Er Tm Yb Lu
b
10000
1000
100
10
1
0.1
0.01
Rock/N-MORB
Cs Rb Ba Th U Nb Ta K La Ce Pr Sr P Nd Sm Zr Hf Eu Ti Gd Tb Dy Y Ho Er Yb Lu

Figure 8

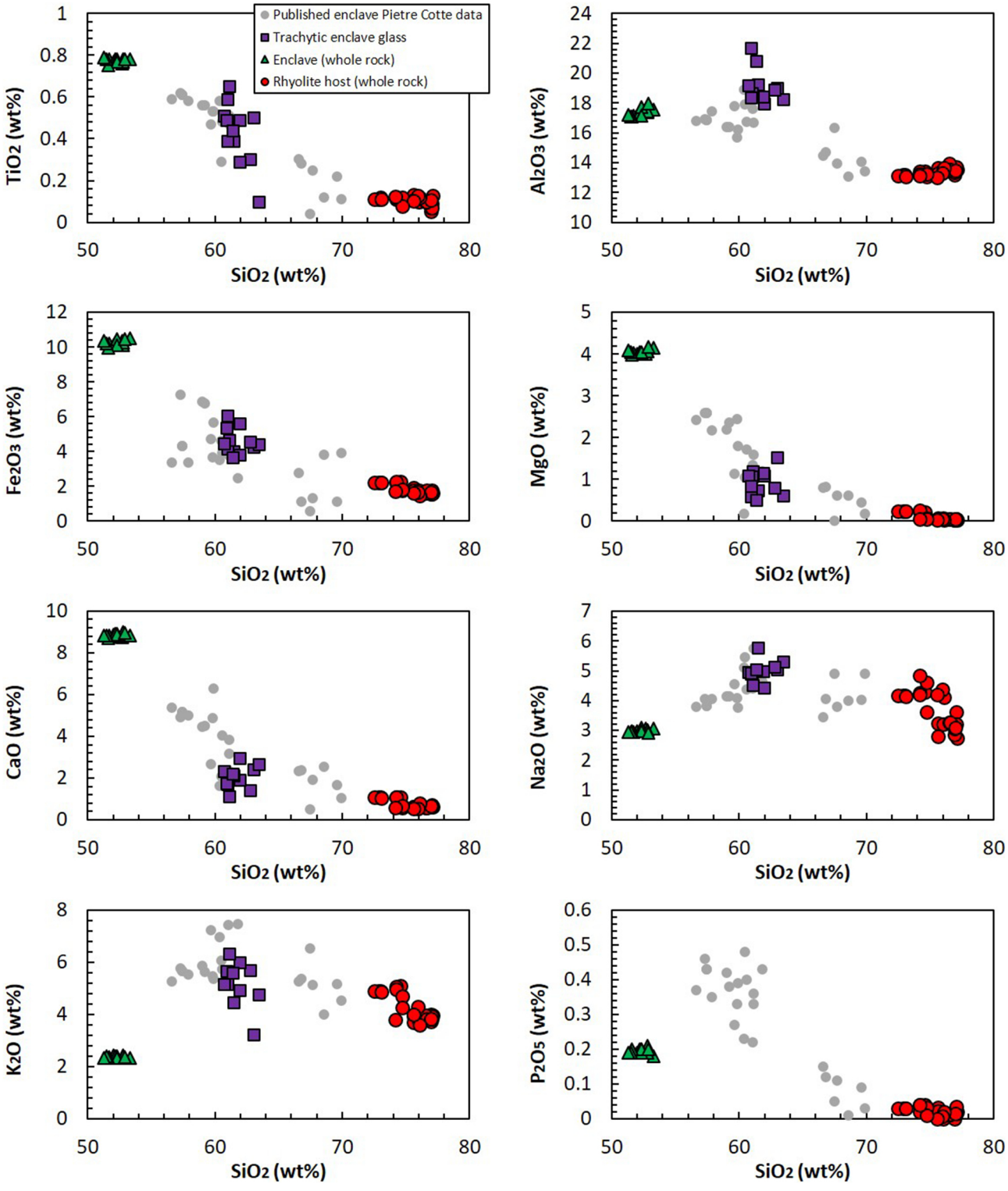
Published enclave Pietre Cotte data
Trachytic enclave glass
Enclave (whole rock)
Rhyolite host (whole rock)
TiO2 (wt%)
Al2O3 (wt%)
Fe2O3 (wt%)
MgO (wt%)
CaO (wt%)
Na2O (wt%)
K2O (wt%)
P2O5 (wt%)
SiO2 (wt%)

Figure 9

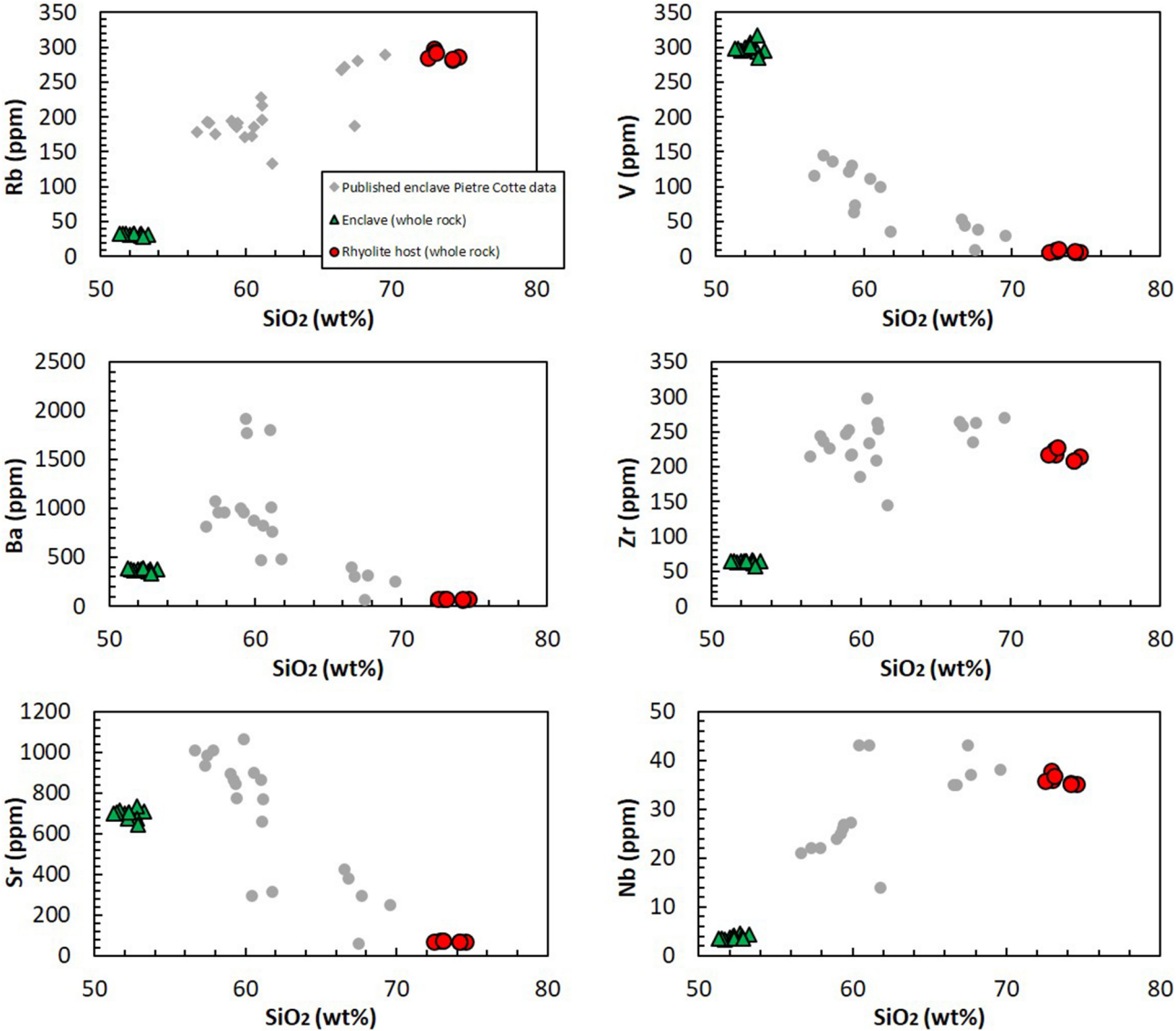
Rb (ppm)
SiO2 (wt%)
Published enclave Pietre Cotte data
Enclave (whole rock)
Rhyolite host (whole rock)
V (ppm)
Ba (ppm)
Zr (ppm)
Sr (ppm)
Nb (ppm)

Figure 10

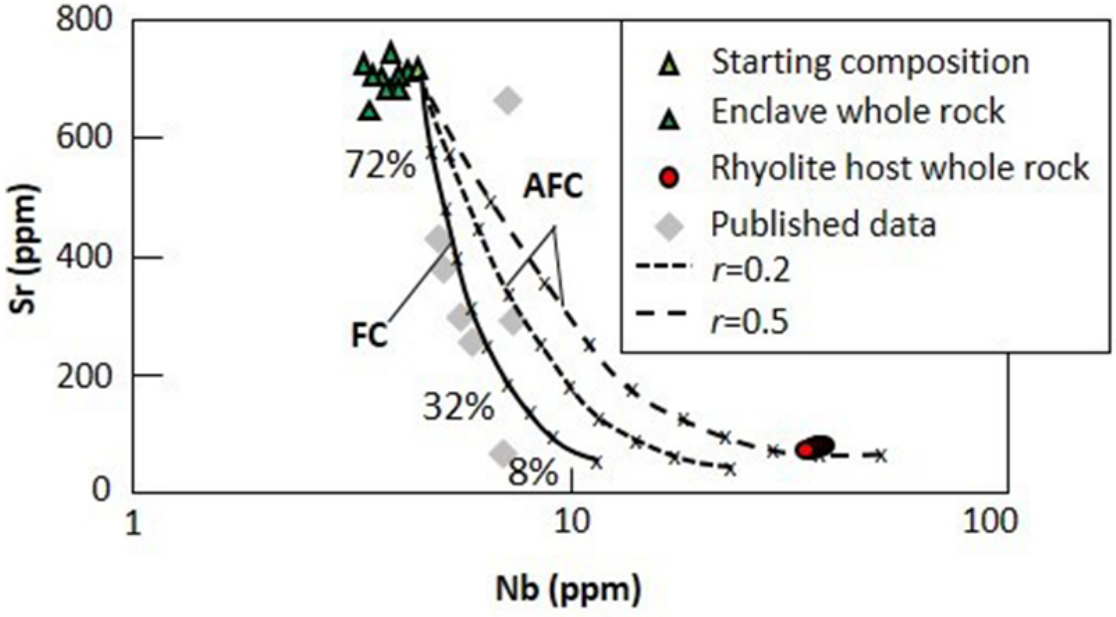
Starting composition
Enclave whole rock
Rhyolite host whole rock
Published data
r=0.2
r=0.5
AFC
FC
72%
32%
8%
Sr (ppm)
Nb (ppm)
800
600
400
200
0
1
10
100

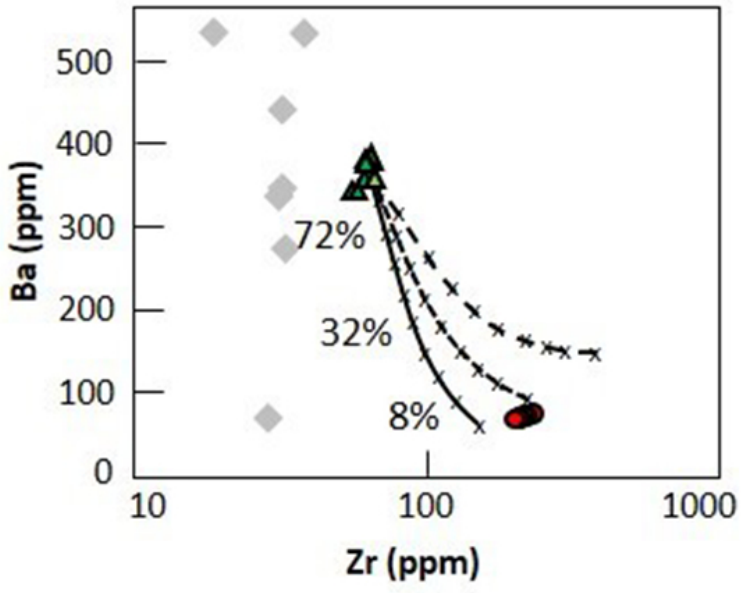
72%
32%
8%
Ba (ppm)
Zr (ppm)
500
400
300
200
100
0
10
100
1000

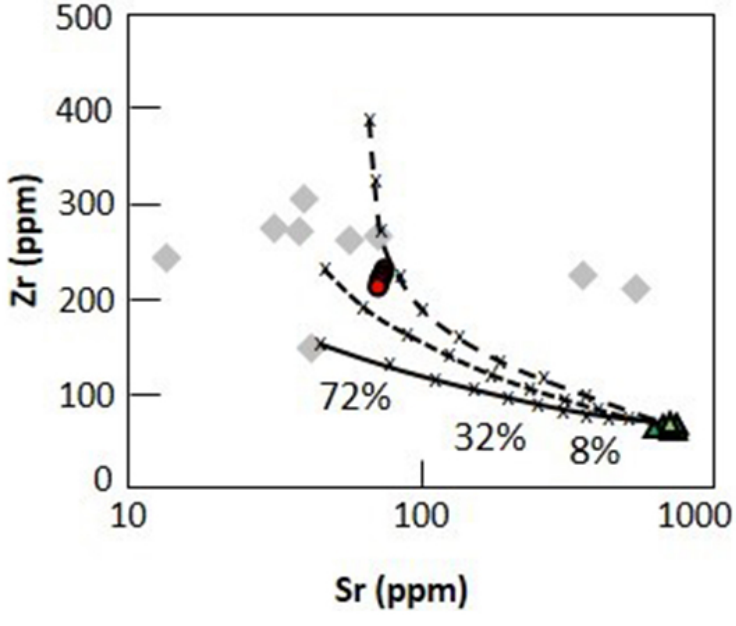
72%
32%
8%
Zr (ppm)
Sr (ppm)
500
400
300
200
100
0
10
100
1000

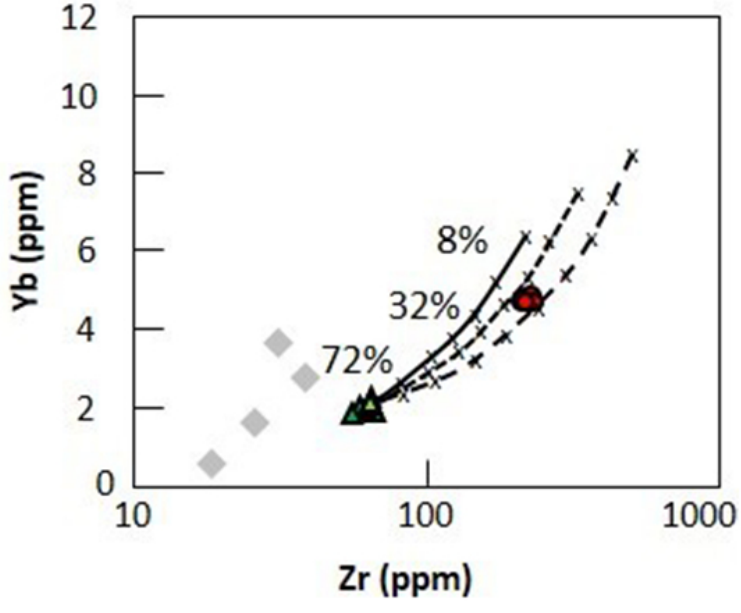
8%
32%
72%
Yb (ppm)
Zr (ppm)
12
10
8
6
4
2
0
10
100
1000

Figure 11

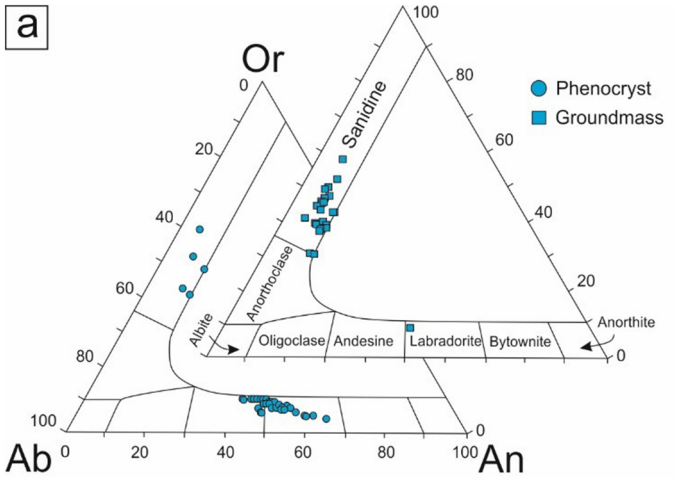
a
Or
Sanidine
Phenocryst
Groundmass
Anorthoclase
Albite
Oligoclase
Andesine
Labradorite
Bytownite
Anorthite
Ab
An

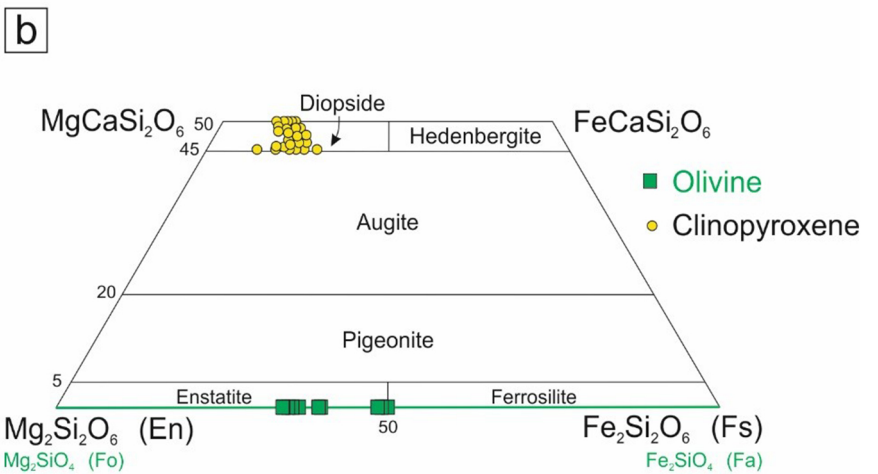
b
MgCaSi2O6
Diopside
FeCaSi2O6
Hedenbergite
Olivine
Clinopyroxene
Augite
Pigeonite
Enstatite
Ferrosilite
Mg2Si2O6 (En)
Fe2Si2O6 (Fs)
Mg2SiO4 (Fo)
Fe2SiO4 (Fa)

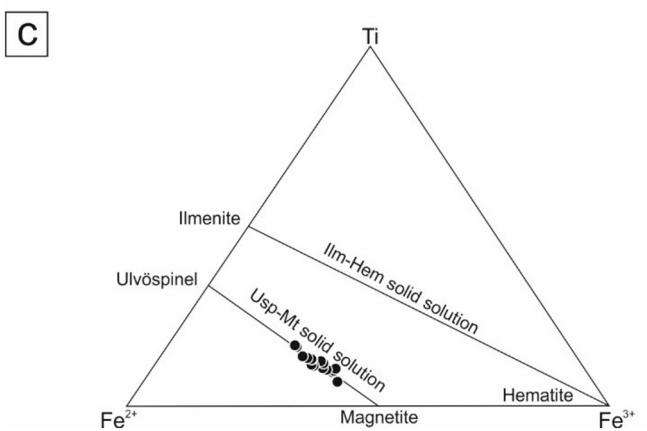
c
Ti
Ilmenite
Ilm-Hem solid solution
Ulvöspinel
Usp-Mt solid solution
Hematite
Fe2+
Magnetite
Fe3+

Figure 12

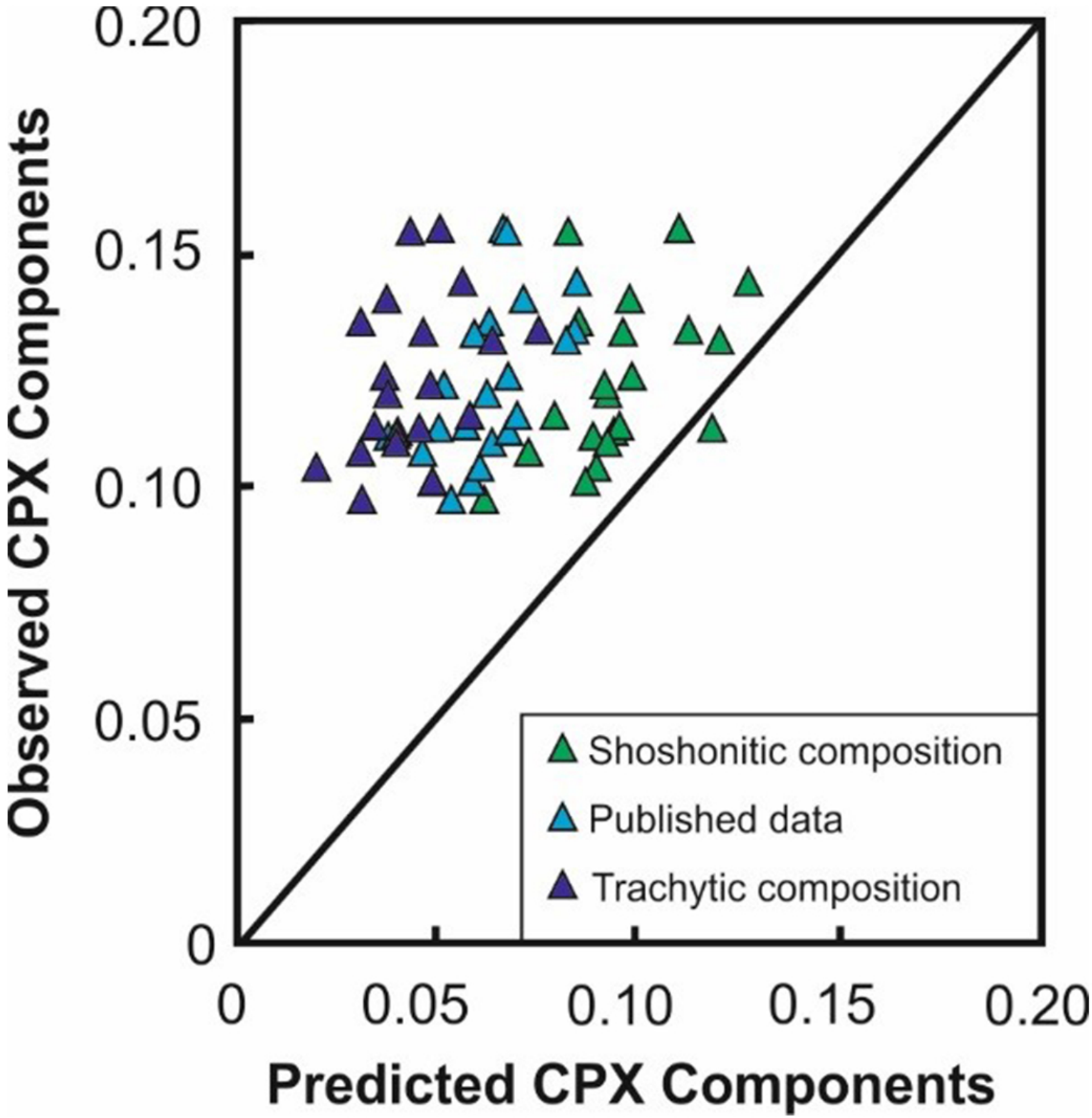
0.20
0.15
0.10
0.05
0
Observed CPX Components
0
0.05
0.10
0.15
0.20
Predicted CPX Components
Shoshonitic composition
Published data
Trachytic composition

Figure 13

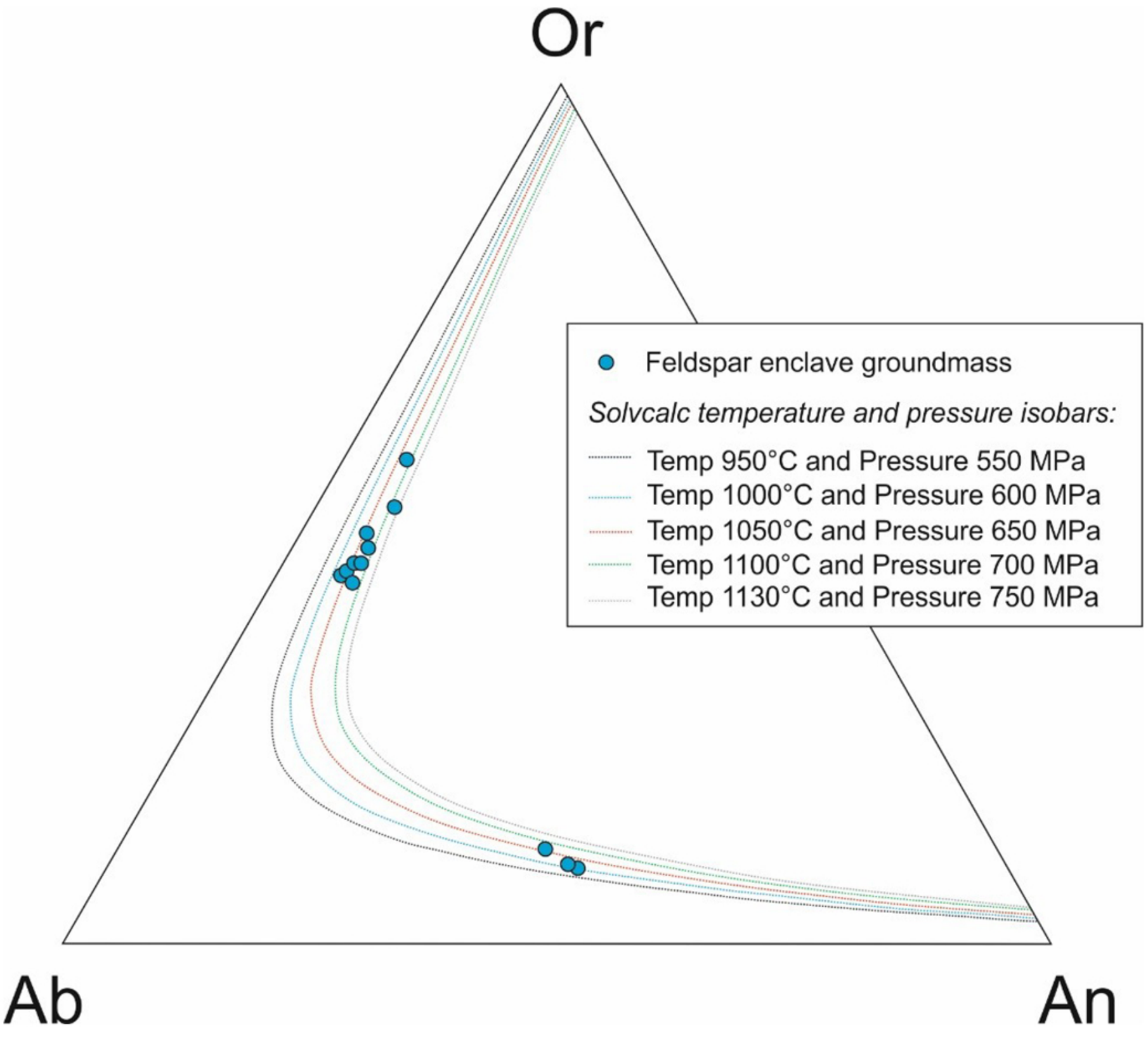
Or
Ab
An
Feldspar enclave groundmass
Solvcalc temperature and pressure isobars:
Temp 950°C and Pressure 550 MPa
Temp 1000°C and Pressure 600 MPa
Temp 1050°C and Pressure 650 MPa
Temp 1100°C and Pressure 700 MPa
Temp 1130°C and Pressure 750 MPa

Figure 14

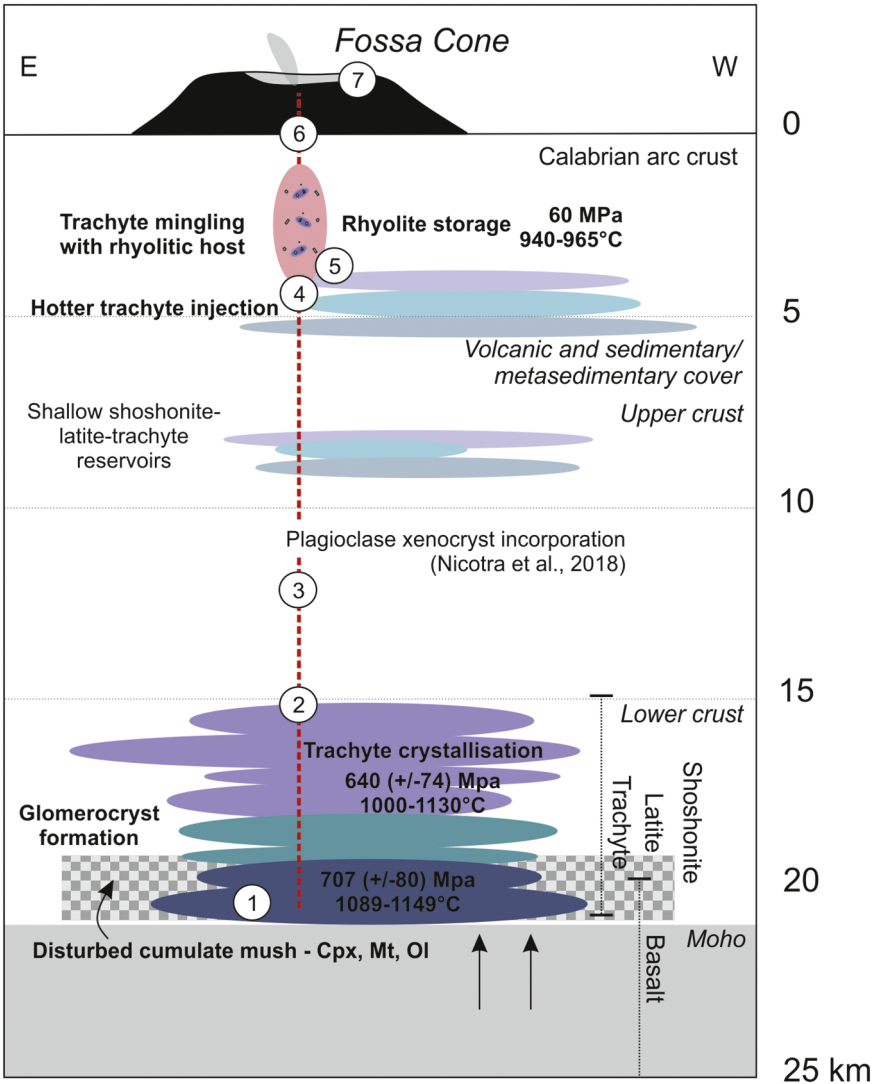
Fossa Cone
E
W
7
6
0
Calabrian arc crust
Trachyte mingling with rhyolitic host
Rhyolite storage
60 MPa
940-965°C
5
4
Hotter trachyte injection
5
Volcanic and sedimentary/ metasedimentary cover
Shallow shoshonite-latite-trachyte reservoirs
Upper crust
10
Plagioclase xenocryst incorporation (Nicotra et al., 2018)
3
15
2
Lower crust
Trachyte crystallisation
640 (+/-74) Mpa
1000-1130°C
Glomerocryst formation
Shoshonite
Latite
Trachyte
707 (+/-80) Mpa
1089-1149°C
20
1
Moho
Disturbed cumulate mush - Cpx, Mt, Ol
Basalt
25 km

Figure 15